Rapid Liquid 3D-Printing of Microchannels using Aqueous Two-Phase Systems:
Towards Vascular Tissue Modelling Applications

by

Joscillyn Poirier

Submitted in partial fulfilment of the requirements
for the degree of Master of Applied Science

at

Dalhousie University
Halifax, Nova Scotia
April 2023

Dalhousie University is located in Mi'kma'ki, the
Ancestral and unceded territory of the Mi'kmaq.
We are all Treaty people.

Table of Contents

List of Tables

List of Figures

Abstract

In vitro models are used to study disease characteristics at a cellular and molecular level. However, conventional modelling techniques have several limitations such as complex fabrication steps, limited scalability, complicated microscopic visualizations of cells, or fail to fully support 3D cultures of cells. To address these issues, this thesis takes a novel approach utilizing rapid liquid 3D-printing (RL3DP) of a biocompatible aqueous two-phase ink and matrix system to create complex tubular structures within a hydrogel matrix where cells can be cultured in physiologically relevant environments for modelling soft tissue. Fluid characteristics, mechanical properties, and cellular viability assays were examined to select polymer concentrations suitable for printing uniform microchannels of 100-1500 μm in diameter. Collectively, the analysis outlined in this thesis supports the applicability of the ink and matrix ATPS systems use for RL3DP applications for soft tissue engineering and disease modelling applications.

List of Abbreviations and Symbols Used

2D	**Two-Dimensional**
3D	**Three-Dimensional**
ANOVA	**Analysis of Variance**
ATCC	**American Type Culture Collection**
ATPS	**Aqueous Two-Phase System**
BBB	**Blood-Brain Barrier**
BD	**Becton, Dickson**
BSC	**Biosafety Cabinet**
CaCl$_2$	**Calcium Chloride**
CAD	**Computer Aided Design**
CNS	**Central Nervous System**
CTB	**Color-Dependent Plot Style**
DEX	**Dextran**
DMEM/F-12	**Dulbecco's Modified Eagles Medium/Nutrient Mixture F-12**
DMSO	**Dimethyl Sulfoxide**
DNA	**Deoxyribonucleic Acid**
ECM	**Extracellular Matrix**
FDM	**Fused Deposition Modelling**
FITC-Dextran	**Fluorescein Isothiocyanate-Dextran**
G'	**Storage Modulus**
G''	**Loss Modulus**
kPa	**Kilopascal**
LCD	**Liquid-Crystal Display**
LUHMES	**Lund Human Mesencephalic Embryonic Stem Cells**
M	**Molar**
Min	**Minute**
MIT	**Massachusetts Institute of Technology**
mL	**Milliliter**

mm	Millimeter
MTT	3-(4,5-dimethylthiazol-2-yl)-2,5-diphenyltetra- zoliumbromide
N	Newton
nm	Nanometer
PBS	Phosphate Buffered Solution
PEG	Polyethylene Glycol
PEO	Polyethylene Oxide
PDMS	Polydimethylsiloxane
RCF	Relative Centrifugal Force
RL3DP	Rapid Liquid 3D Printing
RPM	Revolutions per Minute
s	Second
SLA	Stereolithography
SLS	Selective Laser Sintering
SPSS	Statistical Package for the Social Science
STL	Standard Triangle Language
T_g	Gelation Temperature
T_m	Melting Temperature
TMO	Thermo Fisher Scientific
µl	Microliter
µm	Micrometer
USB	Universal Serial Bus
UV	Ultraviolet
W	Watt
wt.%	Weight Percent

Acknowledgements

I would like to start off by thanking my co-supervisor, John Frampton. This thesis was made possible with your dedicated support, mentorship, and encouragement. I greatly appreciate the time you took to meet with me and trouble shoot the intricate details of this project. I truly would not have made it this far without your knowledgeable input. I would also like to thank my co-supervisor Amyl Ghanem for guiding me through the thesis and providing valuable input. I also want to thank my internal and external committee members Alison Scott and Jong Sung Kim. Acknowledgements to Dalhousie University, Frampton Lab, and the National Science and Engineering Research Council for providing me the resources and funding to complete this research. To all the members of the Frampton Lab, thank you for supporting and encouraging me through every experiment. A huge thank you to my family and friends for the unconditional love and support, I would not have completed this thesis without them. Beginning this MASc during the pandemic took a hard hit on my mental health, I appreciate the love and support from everyone, you all helped boost my mood. Last but not least, a very special thank you goes out to my loving partner who was always there to listen and comfort me through all the highs and the lows of my research and writing experiences.

Chapter 1: Introduction

1.1 Clinical Relevance of *in vitro* Vascular Engineering Models

Various types of diseases that affect soft tissues involve the vasculature system. Neurodegenerative diseases, cancer metastasis, and cardiovascular diseases are all examples of diseases that involve or spread by way of vascular networks. The brain microvascular system has been implicated in numerous neurodegenerative diseases such as Parkinson's disease and Alzheimer's disease, and the presence of a selective barrier in the brain microvasculature can often limit the passage of therapeutics into brain tissues. According to the Alzheimer's Disease Association report for 2022, an estimated 6.2 million people are living with Alzheimer's disease in the United States (Gaugler, et al., 2022). As mentioned above, the treatment of neurodegenerative diseases is often limited by impermeability of blood vessels in the brain, i.e., the blood-brain barrier (BBB), which restricts passage of therapeutic drugs into the central nervous system (CNS) (Sivandzade & Cucullo, 2018). In addition to neurodegenerative diseases, metastatic cancer accounts for approximately two thirds of all cancer deaths in the United States each year (Dillekas, Rogers, & Straume, 2019). Metastasis of cancer cells through the lymphatic system or blood stream spreads the cancer throughout the body, greatly increasing mortality rates. However, the mechanisms surrounding metastasis and exactly why the cancer cells are spread remains unclear, although for cells to metastasize they must interact with the vasculature system (Jaber, 2022). Lastly, heart disease is the leading cause of death, killing approximately 17.9 million people worldwide every year (Cardiovasculature disease, 2023). Narrowing of arteries caused by cardiovascular disease causes weakening of the myocardial tissue, ultimately resulting in myocardial infarction (Matsa, Burridge, & Wu,

1

2014). Being the leading cause of morbidity worldwide, there is an urgent need for better treatment options and drug therapies. Each of the types of diseases mentioned above, and many more, involve the vascular networks present ubiquitously in human tissue. However, researchers have yet to create cell culture models that replicate the intricate geometries of native vasculature. With improved technologies for engineering complex channels within soft matrices, it would become possible to improve patient-specific physiologically relevant *in vitro* modelling of vascular networks to study development and progression of various diseases. Moreover, improved models capable of accurately depicting the true 3D microenvironment of native vasculature would hold tremendous promise for high-content analysis and testing of novel therapeutic drugs for brain disorders and diseases of other soft tissues that involve the vasculature.

1.1.1 Neurodegenerative Diseases and Therapeutics

One major area of interest that drove the research basis for this project is the inability for therapeutic drugs to cross the BBB and penetrate the CNS. The BBB is a highly selective semipermeable barrier which separates the CNS from the peripheral circulation of blood throughout the brain (Logan, et al., 2019). The BBB prevents toxic compounds and pathogens from entering the CNS compartment while also regulating transport of nutrients essential for metabolism of brain cells (Sivandzade & Cucullo, 2018). However, uptake of larger molecules through the endothelium of the BBB is restricted by transporters and many of these molecules are quickly returned from the CNS interstitial fluid back into the blood stream (Sivandzade & Cucullo, 2018). Due to its strict impermeability, many pharmaceutical drugs cannot cross the BBB and penetrate the CNS for treatment of neurodegenerative diseases (Sivandzade & Cucullo, 2018). Therefore, it is of major interest

2

to develop an accurate *in vitro* BBB model equipped to analyze multiple drug candidates before they move to human trials for treatment of neurodegenerative diseases such as Alzheimer's disease (AD), Parkinson's disease (PD), brain cancer, traumatic brain injury (TBI), and Huntington's disease (HD), among the other conditions of the CNS (Logan, et al., 2019).

1.2   Limitations of Conventional *in vitro* Modelling Techniques

Conventional models available to researchers have various advantages and disadvantages regarding their applicability and how well they recapitulate the *in vivo* vasculature of native tissue. Two-dimensional models, such as mono-culture and transwell systems, can be easily constructed and are widely used tools for analysis of cell behavior (Logan, et al., 2019). However, they lack true vasculature geometry and do not incorporate perfusion of media (Logan, et al., 2019). Three-dimensional models, such as dynamic and microfluidic platforms, better represent the *in vivo* environment, but tend to be complicated to construct and sometimes require specialized equipment to operate (Duval, et al., 2017). Novel modelling techniques like 3D-bioprinting utilize bioinks mixed with living cells to create tissue-like 3D structures for cell modelling. However, disadvantages of 3D-bioprinting include lack of precision, inability to print complex structures such as small hollow tubes, high shear stress on cells when printing, and frequent nozzle clogging (Bishop, et al., 2017). This section will discuss in further detail the applications and limitations of each modelling technique and highlight the need for more advanced models to overcome the disadvantages encountered with conventional tissue modelling approaches.

Conventional 2D models require adherence of cells to a flat rigid surface, usually a Petri dish or a transwell insert, which provide a means of support for cells to grow on (Duval, et al., 2017). Two-dimensional modelling results in homogeneous growth of cells as a result of equal access to nutrients and growth factors present within the medium (Duval, et al., 2017). Transwell and mono-culture approaches, as displayed in Figure 1, are used extensively by life scientists due to their low cost, simplicity, and ease of use (Logan, et al., 2019). Additionally, reproducibility of cell differentiation is higher, and it is easier to analyze the cells throughout the differentiation process (Logan, et al., 2019).

Figure 1: Conventional approaches used for cell culture. (A) Transwell model used for cell culture. The image on the left shows the submerged transwell insert and the image on the right shows the transwell insert lifted from the well. (B) Schematic of cells grown as a monolayer on a cell culture plate. Images created with BioRender.com.

However, the simplicity of 2D models comes with many drawbacks surrounding their application in modelling the true architecture of vascular networks. The lack of structure in 2D models is not representative of complex cell-cell interactions found in vascular tissue (Logan, et al., 2019). Although 2D models have distinct advantages for high throughput analysis and differentiation of cells due to their ease of use, they are not adequate for modeling 3D growth patterns and diffusion of compounds from vascular networks into soft tissues.

Dynamic models better represent *in vivo* characteristics and cell-cell interactions of native vasculature by incorporating more than one cell type with continuous perfusion of media (Duval, et al., 2017). As shown in Figure 2, some dynamic models use hollow tubes of microporous fibers to culture different types of cells on the inner (lumen) and outer (abluminal) sides (He, Yao, Tsirka, & Cao, 2014). The microporous structure allows cells to grow in a 3D environment more representative of the microenvironment observed *in vivo* (Sivandzade & Cucullo, 2018). Additionally, the endothelial layer is subjected to constant shear stress induced by fluid flow through luminal channel, which is known to influence the expression of junctional proteins that regulate BBB permeability (He, Yao, Tsirka, & Cao, 2014).
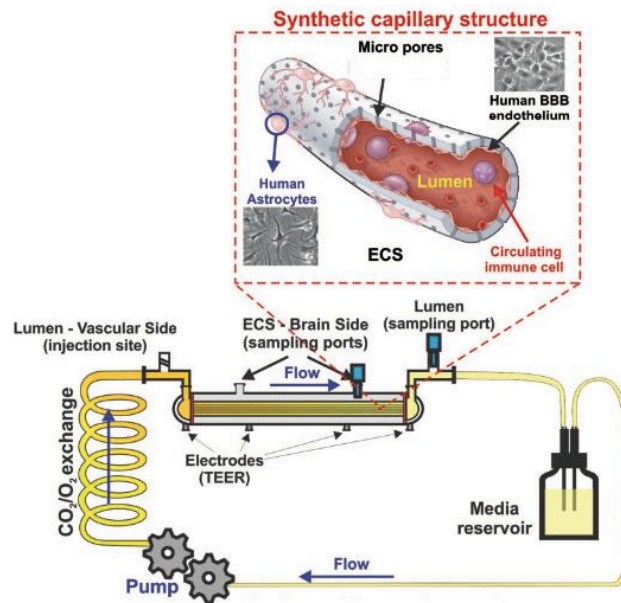
Figure 2: Schematic diagram of a dynamic model of the blood brain barrier. Endothelial cells are cultured inside the hollow fiber structure and astrocytes are cultured on the outside. The fibrous capillary structure is attached to tubing with continuous circulation of media. Images are reproduced with permission from (Sivandzade & Cucullo, 2018).

The luminal flow is generated by a pulsatile pump that can be adjusted to produce physiologically relevant intraluminal pressure similar to what is observed *in vivo* (He, Yao,

Tsirka, & Cao, 2014). Although dynamic modelling has proven to be beneficial in some areas of research, there are several disadvantages that exist. The average thickness of the microporous fibers used in most dynamic models is 150 μm (He, Yao, Tsirka, & Cao, 2014). Therefore, cell-cell interactions between different cell types are limited compared to the immediate contact of these cell types *in vivo*. Additionally, the design of the fibrous tube does not allow for microscopic visualisation of cells (He, Yao, Tsirka, & Cao, 2014). Lastly, there is a high level of technical skill and specialized equipment required for construction of the model that are not readily available to many researchers (Sivandzade & Cucullo, 2018).

To overcome some of these limitations, microfluidic models have been developed that use micro-engineered devices to support the growth of living cell populations to replicate the complex structural features found in native vasculature. Microfluidic models are fabricated on a much smaller scale than transwell or dynamic systems and therefore have more favorable scaling effects including the use of smaller cell populations, shorter diffusion distances between cells in culture, laminar flow comparable to that of the microvasculature, and precise control of nutrient and drug delivery (He, Yao, Tsirka, & Cao, 2014; Kaisar, et al., 2016). As shown in Figure 3, microfluidic models may consist of two crossing microfluidic channels fabricated using soft lithography techniques (He, Yao, Tsirka, & Cao, 2014; Kaisar, et al., 2016).
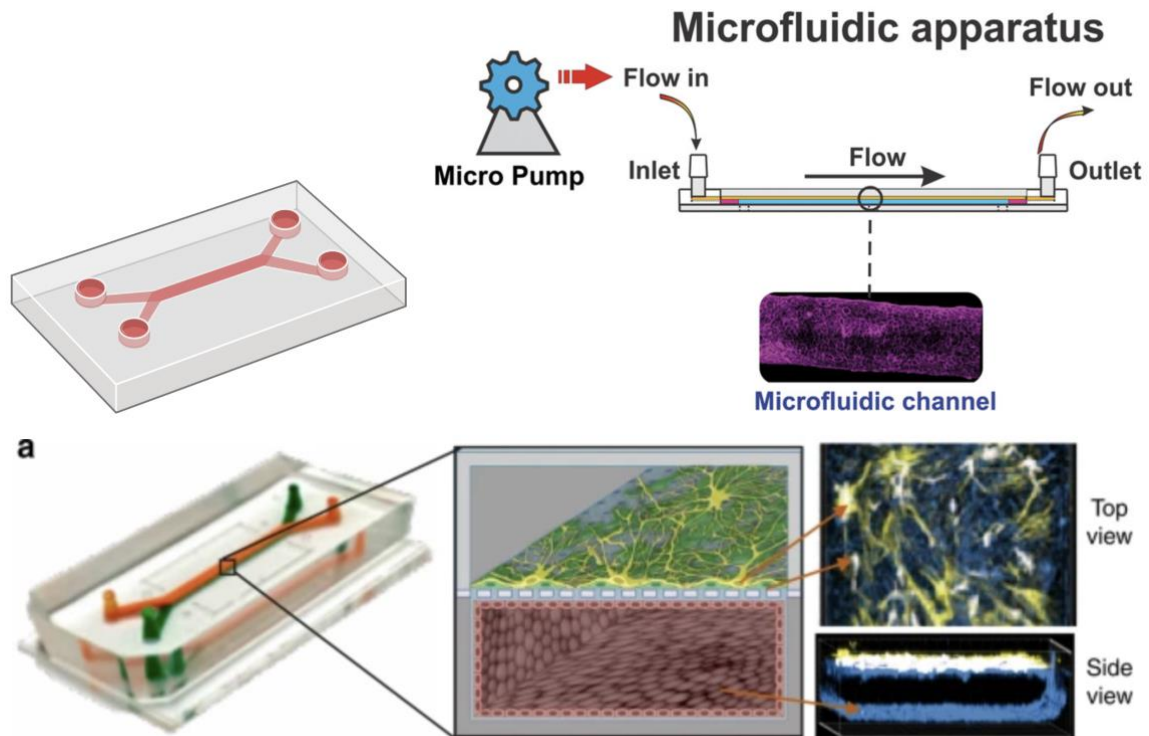
Figure 3: Schematic diagram of a microfluidic cell culture model. Inlet and outlet ports provide continuous flow of media through the luminal compartment of the microfluidic channel. The design and material used for construction of the model allows microscopic visualization of the cells seeded in the channel. Image reproduced with permission from Sivandzade & Cucullo, 2018 and Park, et al., 2019, and modified using Biorender.com.

To fabricate these devices, soft lithography is used, a technique that involves casting an elastomeric polymer, such as polydimethylsiloxane (PDMS), against a photo-patterned master mold of the reverse replica of the microchannel (He, Yao, Tsirka, & Cao, 2014; Kaisar, et al., 2016; Sivandzade & Cucullo, 2018). A polyester or polycarbonate membrane is then used to separate the luminal and abluminal chambers of the two elastomeric relief structures that constitute the microfluidic device, where cell populations can be introduced and allowed to attach to the membrane (Kaisar, et al., 2016). Cells cultured in microfluidic devices can be maintained under either static or dynamic flow to support endothelial barrier formation, cell proliferation, and cell polarization (Kaisar, et al., 2016). Although

microfluidic models are currently the best-performing platform available for modelling vasculature networks, they still have a few disadvantages. Fabrication of microfluidic models use preformed microfabricated models, which require equipment that is not readily available in most life science laboratories (He, Yao, Tsirka, & Cao, 2014). The approach also has limited scalability and although complex structures can be achieved in the x-y planes, it is difficult to achieve complexity in the z-plane (Sivandzade & Cucullo, 2018). Additionally, the PDMS used for fabrication of the microfluidic model can absorb or sequester hydrophobic biomolecules of interest to its surface (Brown, et al., 2015). Overall, microfluidic models most-closely recapitulate *in vivo* characteristics of all current modelling approaches particularly in terms of cellular responses. However, due to the aforementioned limitations, newer modelling techniques involving additive manufacturing techniques are being actively explored.

A newly emerging field of additive manufacturing uses polymer bioinks mixed with living cells to construct 3D structures. Fabrication of tissue constructs with high reproducibility is possible through synchronized crosslinking and bioink deposition with on-the-fly switching of different cell populations (Gungon-Ozkerim, Inci, Zhang, Khademhosseini, & Dokmeci, 2018). Combining additive manufacturing techniques with biocompatible polymer systems supports a wide range of applications for tissue modelling. However, 3D-bioprinting is limited to low viscosity bioinks to reduce the amount of shear stress imposed on cells during the printing process (Bishop, et al., 2017). The crosslinking process is time-sensitive and therefore the hydrogel could substantially deviate from the original design during printing, resulting in poor shape fidelity and printability (Negheih & Chen, 2021). Additionally, creating more complex geometries, such as tubular structures, is not possible due to the lack of structural supports for these features while printing.

1.3   Novel Tissue Model Engineering using Rapid Liquid 3D Printing

Approaches for vascular tissue modelling must support fabrication of complex tubular structures to permit a continuous flow of fluid. Building upon conventional modelling approaches and other additive manufacturing approaches, this thesis will focus on combining microfluidics with 3D-printing to create hollow microfluidic channels of complex designs inside a biocompatible hydrogel network. The microfluidic channels created using this technique can then be infused with cells to create a physiologically accurate multi-cell type model. In order to create such a model, rapid liquid 3D printing (RL3DP) utilizing an aqueous two-phase system (ATPS) has been employed. This approach was developed to overcome the design limitations of conventional modelling techniques. However, in order to create a system using RL3DP to model vascular tissue, an ATPS capable of creating hollow microfluidic channels is required. Details surrounding ATPS and RL3DP are described in the following sections 1.3.1 and 1.3.2, respectively.

1.3.1   What are Aqueous Two-Phase Systems?

Aqueous two-phase systems are formed when two soluble, but incompatible compounds are combined in an aqueous solution above critical concentration required for phase separation to occur (Chao & Shum, 2020). The resulting aqueous mixture yields two separate coexisting phases in equilibrium with one another. When combining two incompatible compounds, their concentrations influence whether the resulting mixture will be miscible or immiscible (Chao & Shum, 2020). Binodal phase diagrams, as shown in Figure 4, delineate the concentration above which the two compounds phase separate.
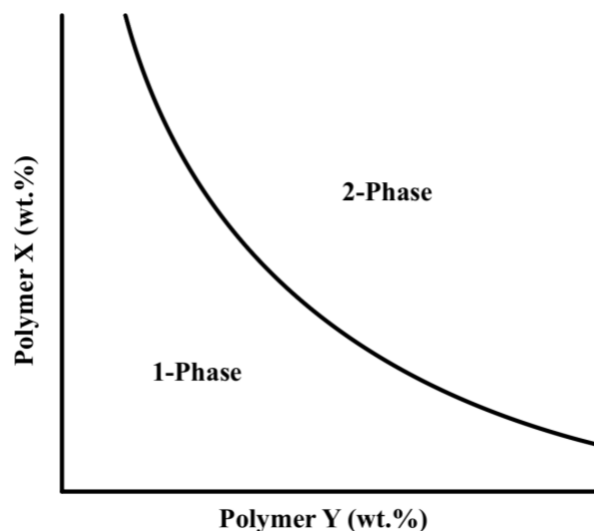
Figure 4: Schematic of a binodal phase diagram. The x- and y-axes represents the respective polymer concentrations. The binodal curve separates the regions where combination of the two polymer solutions results in one or two phases. Below the binodal curve indicates a single miscible solution and above the binodal curve indicates formation of a two-phase system. Redrawn from Chao & Shum, 2020.

The binodal curve separates the concentration of polymers that create a two phase system when mixed together from those that do not. A mixture of polymers below the binodal curve will be miscible and mixtures above the curve will result in a two-phase system with a visible liquid-liquid interface. Aqueous two-phase systems have numerous applications ranging from separation and purification of proteins to biopatterning of cell populations. The most commonly utilized ATPS is formed from polyethylene glycol (PEG) and dextran (DEX). This ATPS has been used for large-scale extraction, separation, purification and recovery of proteins, enzymes, monoclonal antibodies, DNA, nucleic acids, viruses, and metals from various sources (Iqbal, et al., 2016) (Albertsson, 1995) (Frerix, Müller, Kula, & Hubbuch, 2010) (Asenjo & Andrews, 2011). Additionally, ATPS have been used for drug encapsulation for pH-controlled drug release (Zhang, et al., 2018) and ultrasound responsive on-demand drug release (Field, et al., 2022). ATPS have also

been used in cell biopatterning for spatial organization of cells for regenerative medicine applications (Agarwal, Ko, Gratzer, & Frampton, 2017). However, ATPS have only recently become of interest in additive manufacturing. By carefully selecting the materials used to form the ATPS, it may thus be possible to build upon cutting edge additive manufacturing techniques broadly classified as RL3DP (Hajash, Sparrman, Guberan, Laucks, & Tibbits, 2017). Details surrounding RL3DP and current applications are discussed in the next section.

1.3.2   What is Rapid Liquid 3D Printing?

Conventional methods of 3D printing, such as fused deposition modelling (FDM), stereolithography (SLA), and selective laser sintering (SLS), use an imported STL file, slice the model into a multitude of layers, and then print the object layer by layer (Hajash, Sparrman, Guberan, Laucks, & Tibbits, 2017). This process is extremely slow, especially for large objects, and the range of printable materials is limited to curable resins and various plastics (Hajash, Sparrman, Guberan, Laucks, & Tibbits, 2017). Originally developed at MIT's Self-Assembly Lab in 2017, RL3DP is a newly advancing method of additive manufacturing technology that allows users to physically draw any direction in 3D space within a gel suspension (Hajash, Sparrman, Guberan, Laucks, & Tibbits, 2017) (Wood, 2021). As shown in Figure 5 the ink deposited from the RL3DP is held in place by a re-useable bulk gel. Therefore, the user can print any shape without the need for structural supports reducing print time, material waste, and allowing creation of more complex objects (Hajash, Sparrman, Guberan, Laucks, & Tibbits, 2017).
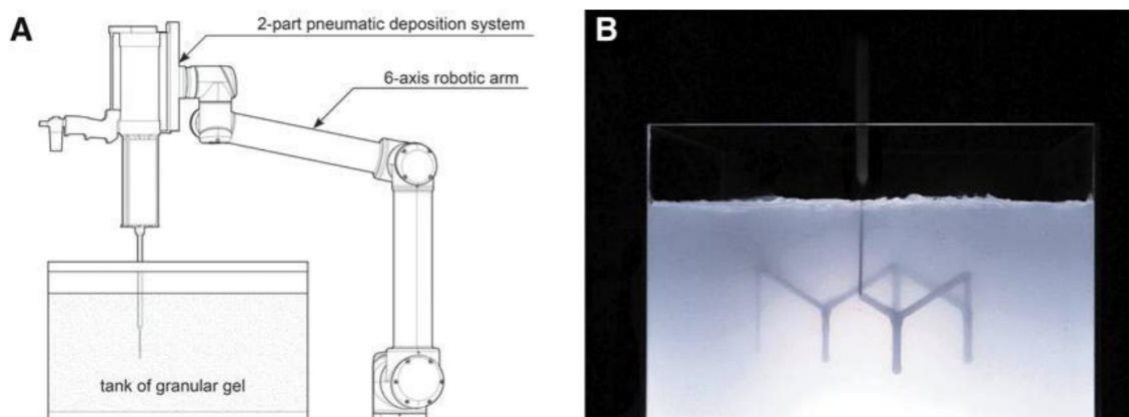
Figure 5: Schematic diagram illustrating the concept of rapid liquid 3D-printing. (A) The RL3DP system used at MIT Self-Assembly Lab. A 6-axis robotic arm and a pneumatic deposition system are used to deposit ink into a tank of granular gel which supports the ink during printing. (B) A complex support-free structure held in place by the granular gel. Reprinted with permission from Mary Ann Liebert Inc. obtained from (Hajash, Sparrman, Guberan, Laucks, & Tibbits, 2017). Illustrations Copyright © Mary Ann Liebert, Inc.

The ink phase is then cured and removed from the bulk phase. Rapid liquid 3D printing is capable of creating objects using various types of materials such as silicones, rubbers, UV curable resins, and cement (Hajash, Sparrman, Guberan, Laucks, & Tibbits, 2017). However, recent publications have incorporated biocompatible polymers with additive manufacturing techniques for applications in tissue modelling and scaffolding.

1.4   Research Goals and Objectives

This thesis outlines the development of an ink and matrix phase suitable for use on a RL3DP to create open microfluidic channels within a biocompatible hydrogel matrix. The RL3DP techniques developed at MIT utilizes curable inks and a re-useable bulk gel to create structures. However, this project takes a different approach to RL3DP by incorporating biocompatible polymers to create channels with sharp boundaries within a bulk gel, essentially the reverse of how RL3DP is typically performed. The overall goal of this project is to design and characterize an ATPS-based ink and matrix phase (to facilitate

formation of smooth channel boundaries by way of the liquid-liquid interface) for RL3DP of complex tubular microchannels inside a biocompatible matrix. In this approach, the printed ink is deposited into a liquid matrix phase which is then stabilized by gelation and crosslinking so that removal of the ink by flushing the channel leaves behind a solidified matrix with a printed network of hollow channels inside. The ink and matrix phase designed for this type of application must consider fluid characteristics such as density, interfacial tension, and viscosity. Additionally, the matrix phase must have gelation and crosslinking characteristics appropriate to maintain the shape of the printed channel once the ink is flushed out. The overall objectives and research goals for this thesis project were as follows:

1. Develop an ATPS-based ink and matrix phase system capable of producing and maintaining uniform microchannels using RL3DP.

2. Design and 3D print a printing chamber to house the ink/matrix combination during printing, allow for microscopic visualization of the printed channel, and attachment to a pump to permit perfusion of liquid media.

3. Develop RL3DP platform capable of creating channels and analyze the relationship between translation speed of the nozzle and volumetric flow rate of the ink on channel diameter and uniformity.

4. Analyze density and viscosity characteristics of both the ink and matrix phase. Furthermore, analyze gelation and melting temperatures, mass loss, elastic modulus, and cell viability of the finalized matrix phase.

It is important to note that my MASc project was a continuation of the research completed in my engineering capstone group project. Throughout the capstone project, we analyzed multiple polymer candidates and performed a wide variety of experimental tests to narrow down suitable polymer combinations. The final combination of phase-separating

polymers was 17.5 wt% PEG/0.1wt.% PEO for the ink phase and 10 wt% gelatin/2wt.% alginate for the matrix phase. It was, however, necessary to extensively optimize this ATPS formulation and the RL3DP approach to create even simple channel structures, and to more rigorously characterize the performance of the approach, thus constituting the original contribution of this thesis.

1.5   Organization of Chapters

This thesis is divided into five main chapters that chronologically address the research process. Chapters 2, 3, and 4 include a brief introduction, materials and methods, and experimental results for each topic addressed. Chapter 2 outlines the developmental process of narrowing down the appropriate polymers and concentrations for both the ink and matrix phases. Chapter 3 discusses development of the printing chamber and RL3DP setup. This chapter also includes images of printed channels and discusses achievable diameters and uniformity of channels. Chapter 4 analyzes the physical and biological characteristics of the ink and matrix phases. More specifically, characteristics such as density, viscosity, mass loss, mechanical performance, and cell viability are discussed in this section. The final section, Chapter 5, highlights potential applications for the modelling technique developed throughout this project and future directions.

Chapter 2: Development and Characterization of Phase Separating Fluids for Rapid Liquid 3D Printing

This chapter focuses on development of the ink and matrix phase formulations used in the design of a system used for rapid liquid 3D printing (RL3DP). Numerous polymer combinations were analyzed in terms of phase separation, biocompatibility, crosslinking, and shear thinning characteristics. The quantitative practices and experiments completed to develop a suitable ATPS combination for RL3DP are discussed in this section.

2.1 Materials and Methodology

2.1.1 Polymer Selection and Justification

Rapid liquid 3D printing is a rapidly advancing subfield of 3D-printing. Only a few research papers published recently have used this printing technique for biomedical applications. Therefore, there is a limited amount of research surrounding the applicability of RL3DP for biomedical applications. For RL3DP to be applied for tissue engineering of vascular structures with sharp boundaries, four major conditions must be met:

1. The ink and matrix phase polymers must form an aqueous two-phase system.

2. The matrix phase must be non-cytotoxic to ensure growth of mammalian cells is not adversely impacted.

3. The matrix phase must stabilize around the ink phase after printing to ensure that removal of the ink phase will create a hollow channel.

4. The ink phase must have shear thinning abilities so it can easily flow through tubing and through the nozzle used for printing.

Numerous polymers were considered and analyzed for this project. Previous research by Peacock, et al. tested phase separation of 68 different polymer solutions and identified

which polymer combinations formed an ATPS. From this list, a select number of biocompatible polymer combinations were further analyzed. These polymer combinations are listed in Table 1.

Table 1: Polymer combinations that form an aqueous two-phase system. Those listed below are typically considered to be non-cytotoxic (Peacock, et al., 2021).

Polymer 1	Polymer 2
Pectin	Gum Ghatti
Pectin	Gum Arabic
Hyaluronic Acid	Gum Ghatti
Hyaluronic Acid	Xanthan Gum
Gelatin	PEG
Dextran Sulfate	Carrageenan (Kappa)
Alginate	Gum Arabic

Of the biocompatible combinations listed above, the list was further narrowed down based on crosslinking and gelation capabilities. Phase separating systems made from gelatin/PEG and gum arabic/alginate can be stabilized by gelation and crosslinking, respectively. Gelatin is widely known to melt when heated and solidify at room temperature (Djagny, Wang, & Xu, 2001). Furthermore, alginate can be crosslinked in the presence of divalent cations, such as calcium. Calcium interacts with the polyguluronic acid units of alginate forming an insoluble hydrogel (Chan, Jin, & Heng, 2002). A matrix phase composed of gelatin and alginate can thus facilitate stabilization of the hydrogel network by gelation and crosslinking. Gelation of the matrix phase before crosslinking of the alginate is required to maintain shape of the cylindrical specimen. Crosslinking of an alginate solution by itself results in imperfections to the surface of the hydrogel. Additionally, gelation of the gelatin solution alone is not sufficient for long term use in cell culture conditions as the gelatin degrades overtime. Therefore, it is important to have both

gelation and crosslinking abilities to ensure the matrix phase forms properly and also maintains shape overtime.

The melting temperature of gelatin is dependent on the gel strength designated by the degree of Bloom (Djagny, Wang, & Xu, 2001). Higher Bloom gelatins have higher melting temperatures whereas low Bloom gelatins have much lower melting temperatures. When low Bloom gelatin hydrogels are placed inside an incubator at 37 °C, they typically lose their structure rapidly in the absence of an additional hydrogel network or crosslinking. Therefore, the highest Bloom gelatin of ~300g Bloom was used for this project.

PEG and gum arabic phase separate with gelatin and alginate, respectively, making them suitable candidates for the ink phase. Preliminary printing experiments using gum arabic as the ink phase and a mixture of gelatin and alginate as the matrix phase produced channels with distorted boundaries likely due to its binding properties. However, when using PEG as the ink phase, clear boundaries were observed. Therefore, PEG was chosen as the main component of the ink phase. PEO, a non-Newtonian polymer, was added to increase the shear thinning properties of the ink phase to reduce pressure build up inside the tubing to the print head. Table 2 displays the final polymers chosen for both the ink and matrix phases. However, to identify polymer concentrations best suitable for this system, further analysis of polymer characteristics such as density, critical concentration for phase separation, and interfacial tension was required. An overview of the process taken to finalize the ink and matrix phase compositions is displayed (see Appendix B: Supplementary Tables; Table B2).

Table 2: The final polymers chosen for both the ink and matrix phases along with their respective manufacturer, molecular weight, and roles in the printing process.

Component	Polymer	Manufacturer	M$_W$	Role
Ink	PEG	Sigma-Aldrich (81310)	35,000	Phase separation
	PEO	Sigma-Aldrich (372838)	8,000,000	Shear-thinning
Matrix	Gelatin	Sigma-Aldrich (G1890)	~ 300 Bloom	Phase separation and gelation characteristics
	Alginate	Sigma-Aldrich (71238)	-	Crosslinking ability

2.1.2 Polymer Preparation

The methods described in this section refer to the creation of polymer formulations for both the ink and matrix phase, unless otherwise explicitly stated.

2.1.2.1 Preparation of Non – Sterile Polymer Solutions

Polymer solutions for the ink and matrix phases were made by mixing polymer powder with an aqueous solvent. Prior to preparing the solutions, the desired mass of polymer in weight percent (wt.%) and the corresponding volume of solvent was calculated. The desired amounts of polymer were weighed out and transferred to a Falcon tube containing the desired amount of DMEM/F-12 (aqueous media used for cell culture). The solutions were homogenized following the process outlined in section 2.1.2.4. These solutions were used for characterization in the absence of cells.

2.1.2.2 Preparation of Sterile Polymer Solutions

Prior to preparing the solutions, the desired mass of polymer in weight percent (wt.%) and the corresponding volume of solvent was calculated. Separate polymer powder containers were purchased and only used to make sterile polymer solutions in the biosafety

cabinet (BSC) to ensure sterility of polymers was maintained. Additionally, a portable high precision scale was used to measure out polymer amounts inside the BSC to maintain sterility and avoid frequent traffic in and out of the BSC. The BSC was decontaminated thoroughly with 70% ethanol beforehand. Supplies required to prepare the polymer solutions such as polymer powder containers, Falcon tubes, scoopulas, tube racks, media, and portable scale were gathered and placed on the lab bench nearest the BSC on a sterile towel. Each item was sprayed thoroughly with 70% ethanol before being placed inside the BSC. Once all items were in the BSC, polymer solution preparation began. A single test tube rack with an open Falcon tube was placed on the scale and tared to zero. The mass of polymer powder was weighed out using a scoopula and placed directly into the Falcon tube. Once the desired amount of a polymer was weighed out, the scoopula was sprayed with 70% ethanol and wiped clean with a Kim wipe. The scale was tared again before measuring the next polymer. Once all polymer powders were weighed, sterile DMEM/F-12 was added to the Falcon tube. The cap was replaced on the Falcon tube and homogenized following the process outlined in section 2.1.2.4.

2.1.2.3 Preparation of Sterile Crosslinked Cylindrical Matrix Phase Specimens

The initial polymer preparation followed the steps outlined in section 2.1.2.2. Once the polymer solutions were homogenized and centrifuged, the Falcon tube was sprayed with 70% ethanol and placed inside the BSC. The cylindrical specimens produced were 10 mm in height and 22.8 mm in diameter with a flat surface on the bottom and the top formed a meniscus of 0.5-1mm in height. Supplies required to prepare the specimens such as 12-well cell culture plates, micro spatula, syringe cap, and a 30 mL sterile syringe were placed on the lab bench nearest the BSC on a sterile towel. Each item was sprayed thoroughly with

70% ethanol before being placed inside the BSC. The syringe was removed from its packing and the plunger was detached and set to the side. A syringe cap was placed on the tip of the syringe to ensure no polymer leaked out during transfer. The polymer solutions were transferred from the Falcon tubes to the syringe tubes by pouring the contents and a micro spatula was used to collect the remaining polymer stuck to the sides of the Falcon tube. Once all polymer was transferred, the plunger was attached to the syringe and flipped over to allow the air bubble to reach the syringe tip. The cap was removed, and the plunger was pushed until no air bubbles remained inside the syringe. The 12-well plate was removed from its packaging and the lid was placed to the side. The syringe containing the polymer solution was used to measure and deposit 2.0 mL of matrix phase into each well of the 12-well plate. Once all wells in the plate contained matrix phase, the lid was replaced, and the plate was left to sit in the BSC on a flat level surface at room temperature for 30 minutes until the matrix phase partially gelled. To ensure the matrix phase fully gelled, plates were carefully transferred to a 4°C refrigerator for an additional 10 minutes. Once fully gelled, the plates were sprayed with 70% ethanol and placed back into the BSC at room temperature. To crosslink the specimens, a pipette was used to deposit 2.0 mL of 0.1 M $CaCl_2$ solution dissolved in DMEM/F-12 into each well and the samples were left to crosslink at room temperature for 20 minutes to ensure entire specimen was crosslinked. Once crosslinked, the $CaCl_2$ solution was removed, and each specimen was rinsed three times with PBS to ensure no excess crosslinking solution remained. Before the samples were placed in an incubator at 37 °C, 1.0 mL of DMEM/F-12 with 1% Antibiotic was added to each well.

2.1.2.4 *Homogenization of Polymers*

To facilitate homogenization of the polymer solutions, the solutions were vortexed at 3000 rpm until the polymer powder was uniformly distributed throughout the solvent and then the solution was placed in a water bath at 37 °C for at least 1 hour. To further aide in homogenization of the polymer solutions, the solutions were loaded into a syringe connected to a second syringe using a female-female Luer lock connecter. The solutions were pushed from one syringe to another. This process was repeated ~20 times to ensure complete homogenization of the polymer solution. Once homogenized, the solutions were transferred back to a Falcon tube and centrifuged for 2 minutes at 1400 RCF to remove unwanted air bubbles. This is a universal method for homogenization of polymers and does not impart polymer degradation or any sorts.

2.1.3 Gelatin and PEG Binodal Phase Diagram

Binodal phase diagrams were used to identify compositions that phase separated. Twenty milliliter stock solutions of 20 wt.% gelatin and 5 wt.% PEG were prepared using the process outlined in section 2.1.2.1. The binodal analyzed gelatin and PEG concentrations of 0.5-20 wt.% and 0.5-5 wt.%, respectively. This range was selected based off of previous binodal experiments of gelatin and PEG. A Falcon tube with DMEM/F-12 was used as the solvent. The Falcon tubes containing polymer solutions were kept in a water bath maintained at 37 °C throughout the experiment to ensure temperature fluctuations did not influence phase separation. Additionally, the 96-well plate used for the experiment was kept on a 200 W Cozy Products warming plate on medium heat to avoid cooling of the mixture. Each well of the 96-well plate was used for individual experiments testing desired concentrations of polymer together to see if they resulted in a 2-phase

system or one continuous phase. The final volume for each experiment was 200 μl. The contents of each well were pipetted up and down 4-5 times using a 200 μl pipette to ensure the polymers were mixed thoroughly. The resulting mixture was left to rest for 30 seconds on the warming plate and then inspected under a microscope to observe droplets indicative of phase separation. If no droplets were present, the composition was deemed not to have phase separated. Each phase separating combination was further diluted in separate experiments by 1 wt.% increments with DMEM/F12 until no droplets were present. This process was repeated for various compositions until the concentration that last formed two phases were taken as data points to fit the binodal curve.

2.1.4 Density

Factors such as polymer concentration and temperature influence density of each phase. Polymer solutions were prepared using the process outlined in section 2.1.2.1 and kept in a water bath at 50ºC. An Anton Paar DMA 35 Density Meter was used to measure the density and corresponding temperatures of the polymer solutions. When running a test, the plunger on the density meter was used to collect ~3.0 mL of polymer solution through the tubing into the device. It was crucial to ensure that no bubbles entered the device as that would generate unreliable density readings. As the polymer within the device began to cool down, density readings and their corresponding temperatures were recorded. Once all recordings were captured for one polymer concentration, the device was flushed with a syringe containing hot water three times to calibrate the device and remove any remaining polymer from inside the device before the next test was performed.

2.2 Experimental Results and Discussion

2.2.1 Gelatin and PEG Binodal Phase Diagram

The binodal curve defines the specific polymer concentrations where phase separation between polymers is thermodynamically favorable (Iffah, Arshad, & Amid, 2018). Figure 6 displays the binodal phase diagram for gelatin and PEG.
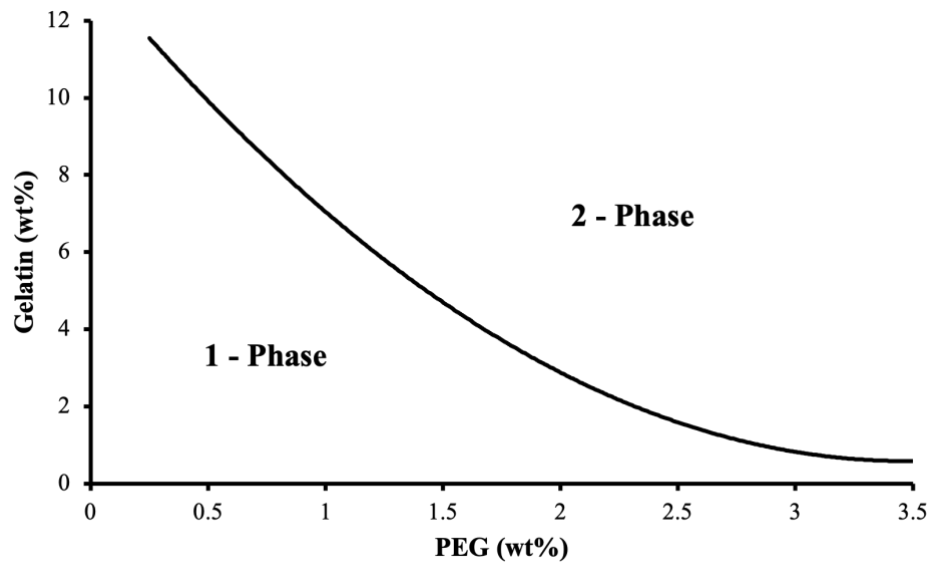
Figure 6: Binodal phase diagram for gelatin and polyethylene glycol. The curve indicates the critical region between a 1-phase system and a 2-phase system. The curve defines the specific compositions of gelatin and PEG at which phase separation is thermodynamically favorable.

The binodal curve illustrates polymer combinations that result in either 1-phase or 2-phases for the specific polymer formulations used in this application. This phase diagram permitted selection of formulation for RL3DP.

2.2.2 Interfacial Tension

ATPS combinations further away from the binodal curve have increasingly large interfacial tension between separating phases (Antonov, Puyvelde, & Moldenaers, 2004). Droplet breakup occurs when the interfacial tension between polymers is large and forces

the ink phase to drop to its lowest energy state, a sphere (van der Graaf, Schroën, van der Sman, & Boom, 2004). Comparing the initial ATPS combination from the capstone project of 17.5 wt.% PEG and 10 wt.% gelatin to the binodal curve shown in Figure 6, these concentrations result in a point very far from the binodal curve in the two-phase region. Figure 7 shows the process of the ink phase breaking up and forming spheres over a period of 10 minutes.
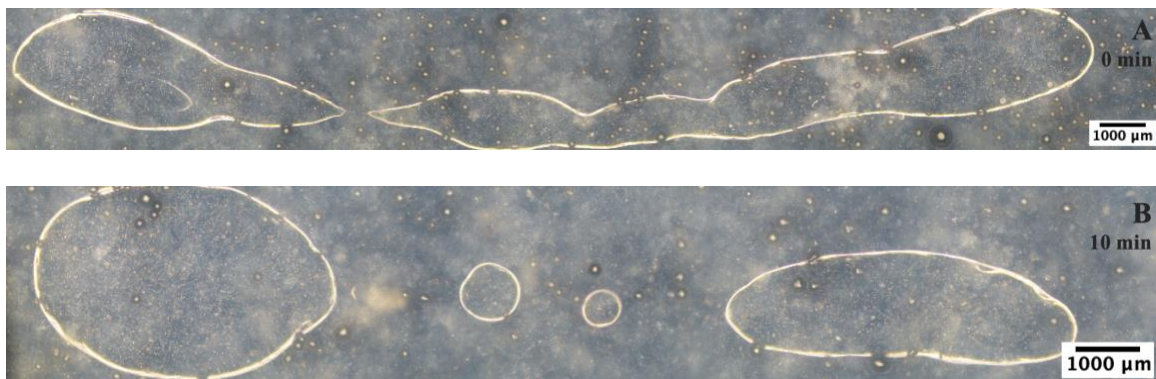

Figure 7: A channel printed using a non-optimized ink and matrix phase combination of 17.5 wt.% PEG/0.1 wt.% PEO and 10 wt.% gelatin/2 wt.% alginate, respectively. Images A and B display the process of ink droplet break up due to high interfacial tension between separating phases. (A) Image of the channel immediately after printing. (B) Image of the channel 10 minutes after printing.

Droplet breakup is unfavorable for the application of RL3DP as the channels do not form properly. Therefore, the concentrations of phase separating polymers were re-evaluated to combat this issue. To ensure the final matrix phase still possessed gelation characteristics, the gelatin concentration was only lowered to 5 wt.%. The corresponding concentration of PEG was determined by analyzing the binodal phase diagram. It is important to note that incorporation of additional polymers will slightly shift the binodal curve. Therefore, choosing a point too close to the binodal curve could cause a two-phase system to become one phase. The final concentrations chosen for the new ATPS formulation were 5 wt.% gelatin and 2.5 wt.% PEG. These concentrations were close to the

binodal curve but far enough into the two-phase region to ensure phase separation was maintained even with additional polymers present. Figure 8 displays a channel printed with the new ATPS combination of 2.5 wt.% PEG / 0.1 wt.% PEO and 5 wt.% gelatin / 2 wt.% alginate for the ink and matrix phase, respectively.
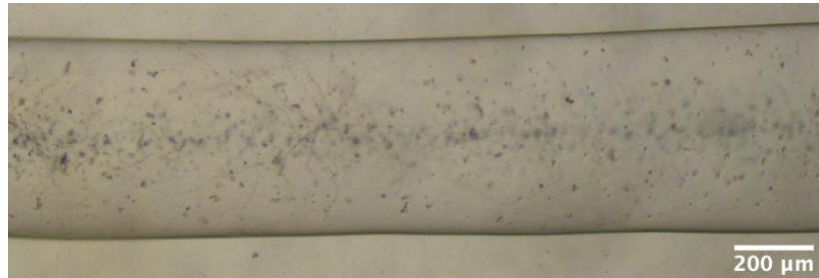
Figure 8: A channel printed using an ink and matrix phase combination of 2.5 wt.% PEG/0.1 wt.% PEO and 5 wt.% gelatin/2 wt.% alginate, respectively.

Although droplet break up no longer occurred, the new formulation resulted in a dramatic difference in density between the phases causing the ink to float to the surface of the matrix phase shortly after printing. The next section thus focuses on optimizing density.

2.2.3 Density

Density is a very important fluid characteristic for this project. A dramatic difference in density between the ink and matrix phase would cause sinking or floating of the ink phase during printing, ultimately compromising the final print. Figure 9 displays a schematic of what would happen during the printing process if the density of the ink is higher, the same as, or lower than the density of the matrix phase.
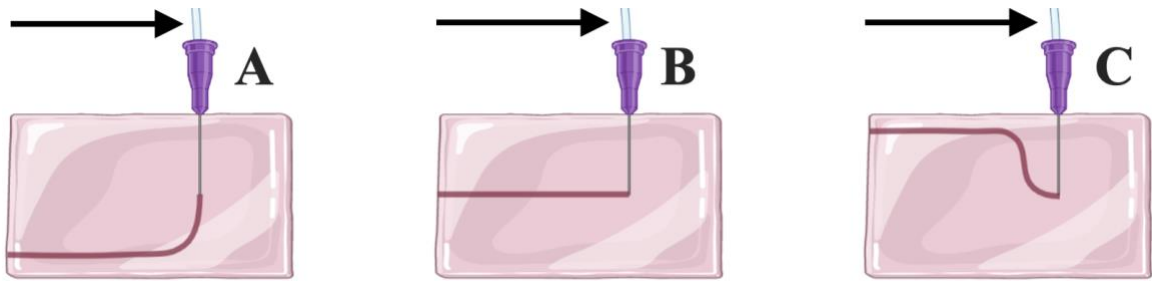
Figure 9: A schematic drawing depicting the results of printing while using an ink that has (A) higher or (C) lower density than the surrounding matrix phase. (B) Displays the result when printing with an ink that has the same density as the surrounding matrix phase. The arrows demonstrate the direction of movement of the printhead while printing. Schematic created with BioRender.com.

This RL3DP system requires the temperature to be changed for gelation of the gelatin. Fluctuations in temperature directly influence the overall density of both the ink and matrix phase. In addition to temperature, polymer concentrations also have a major influence on density. This made it difficult to design an ink phase that remained neutrally buoyant inside the matrix phase. Figure 10 displays the relationship between density, temperature, and concentration for PEG, PEO, alginate, and gelatin, the polymeric components of the ink and matrix phases.
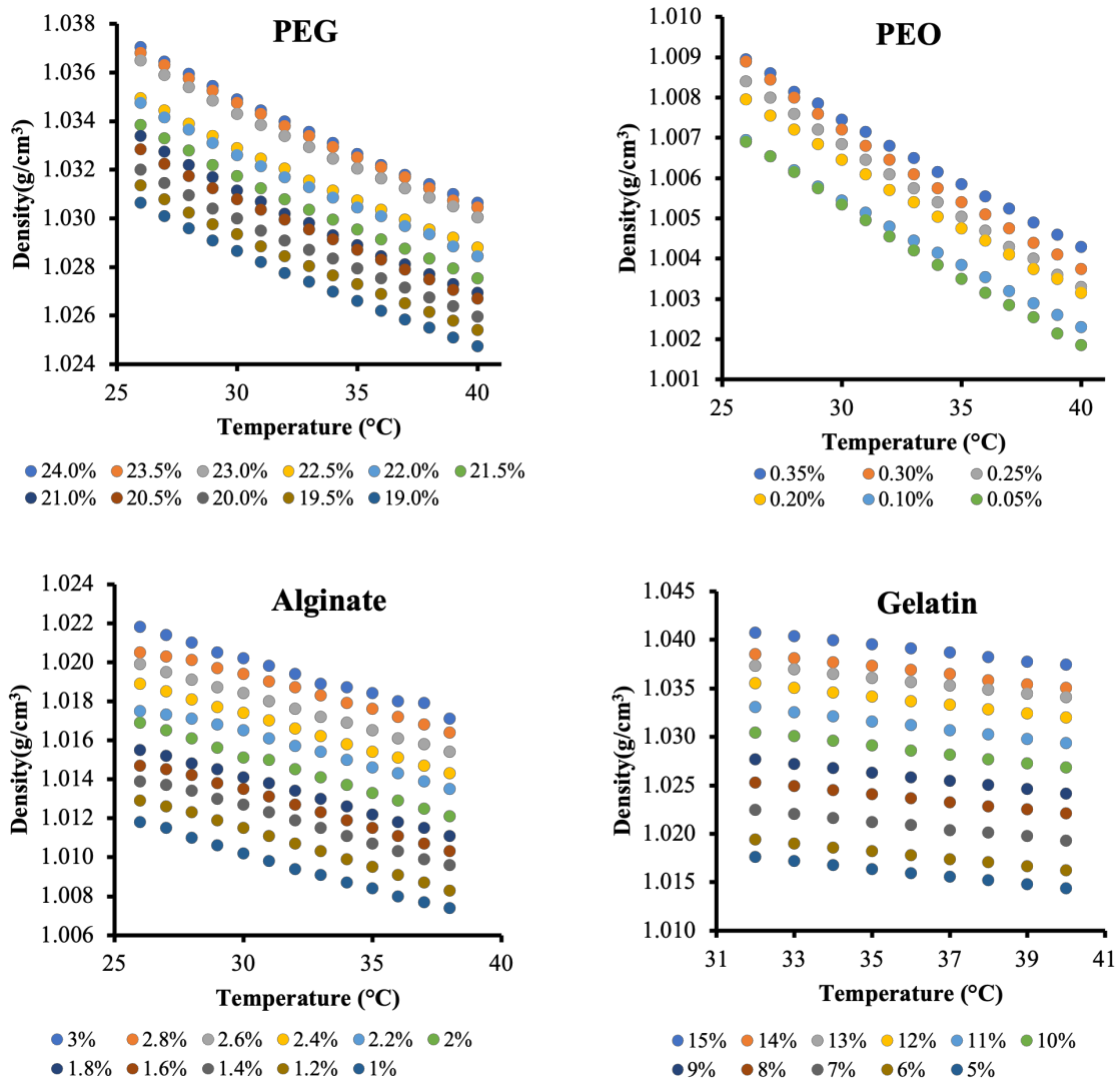
Figure 10: Graphs of density vs. temperature vs. concentration for polyethylene glycol (PEG), polyethylene oxide (PEO), alginate and gelatin. Each color series on the graph represent a different concentration of that polymer.

This experiment identified the range of densities achievable for each polymer within the system at specific temperatures and concentrations. However, when combining the polymers together to create the ink and matrix phases, the resulting densities changed because there was more polymer per unit volume of the mixture.

Trying to balance density, interfacial tension, concentration, and phase separation of polymers proved tedious, and would require re-optimization if any component of the

system were to be modified in the future. Moreover, any alterations of polymer concentration would directly impact the density, interfacial tension, and phase separation of the overall system. Elimination of density as a constraint would thus dramatically simplify the approach. Since the concentration of polymers must be high enough to achieve phase separation, but not too high to result in droplet breakup, the only constraint able to be eliminated was density. It was thus hypothesized that adding a high-density reagent to both the ink and matrix phase would increase the overall density of the system such that the individual polymer contributions to density would be negligible.

The best candidate to increase density was sucrose. Sucrose is a naturally derived disaccharide composed of glucose and fructose, which has been used previously in ATPS formulations to adjust density of one of the phases (Ko, et al., 2020). Three sets of ink and matrix phase polymer solutions were made with varying concentrations of sucrose: 10wt.%; 20 wt.%; 30 wt.%. All sucrose concentrations in the ink phase were tested with all sucrose concentrations in the matrix phase for a total of 9 experiments. For each experiment, approximately 5mL of matrix phase was added to a clear test tube submerged in a water bath kept at 37 °C. To identify which combination of ink and matrix phase would eliminate sinking or floating of the ink phase, ~5 μl of each ink phase was deposited directly in the middle of the matrix phase solution. Test tubes were removed from the water bath and left at room temperature for ~30 minutes to allow gelation of the matrix phase. It was observed that 20 wt.% sucrose in the matrix phase and 30 wt.% sucrose in the ink phase produced droplets of ink that remained neutrally buoyant inside the matrix phase. Additionally, channels printed with this concentration remained neutrally buoyant and were uniform in shape. Table 3 displays the finalized ink and matrix phase compositions for this project.

Table 3: The finalized concentrations of polymers in both the ink and matrix phase. Concentrations are displayed in wt.%.

Ink		Matrix	
	2.5 wt.% PEG		5 wt.% Gelatin
	0.1 wt.% PEO		2 wt.% Alginate
	30 wt.% Sucrose		20 wt.% Sucrose

Addition of sucrose to the ink and matrix phases eliminated density as a constraint to the system and resolved the sinking and floating issue during printing. The concentration of polymers within the system was finalized and the project was able to move on to the next phase of testing.

2.3   Chapter Summary

Characteristics such as phase separation, interfacial tension, and density of polymer solutions were analyzed. Based on experimental results, concentrations and combinations of polymers were fine-tuned to create an ATPS capable of producing high resolution channels inside a biocompatible matrix phase. Droplet breakup of the ink was corrected by lowering polymer concentrations which decreased interfacial tension between separating phases. Floating and sinking of the ink during printing was resolved with the addition of sucrose to both phases which balanced the overall density of the system. Overall, analyzing characteristics of the ATPS provided key information about how to finalize the overall make-up of the ink and matrix phases.

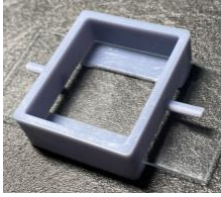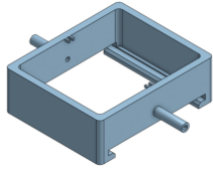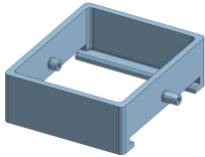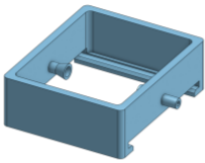# Chapter 3: Rapid Liquid 3D Printing of Ink and Matrix Phase Polymers and Analysis of Printed Structures
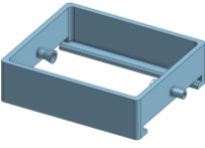
This chapter focuses on RL3DP of microchannels within a phase separating matrix phase. The materials and procedures used to build a RL3DP and achieve proper formation of channels are explained in this section. The design and development of the printing chamber used to house the matrix phase while printing and the process of imaging printed channels is also described. The results of this section outline the various channel designs and dimensions that can be achieved by this approach.

3.1 Materials and Methodology

3.1.1 Development and Design of the Channel Printing Chamber

Rapid liquid 3D printing consists of a bulk phase contained inside a tank and a print head which moves throughout the bulk phase extruding ink and creating the desired print. In most RL3DP applications, the ink is cured and removed from the bulk phase. However, for this project, the bulk phase is stabilized by gelation and crosslinking of the matrix around the ink to create a hollow vascular-like network. The hydrogel bulk phase and the network of channels can be seeded with cells to create customized soft tissue models. For this application, a specialized device compatible with RL3DP was required to contain the bulk phase during the printing process, but also allow for microscopic visualization and perfusion of media throughout the channels afterwards. Design of this printing chamber changed substantially over the course of this project to account for various challenges in ink and matrix phase design that were encountered. The key design features and modifications to the printing chamber are outlined in Table 4.

Table 4: Design process for manufacturing the printing chamber. The key design features, image of printing chamber design, design flaws of that printing chamber design, and the subsequent modifications of design are displayed.

#	Design Features	Image	Design Flaws	Next Modification
1	- Bottom of chamber designed for addition of glass slide after printing. - Ports on outside of the chamber for tubing attachment.		- Glass attachment design snug. - Hard to line up print head to port when printing.	- Bottom of chamber was modified for easier addition of glass slide. - Port indicators were added.
2	- Bottom of chamber easily fit glass slide after printing. - Port indicators helped locate port to line up channel correctly.		- Port indicators interfered with printing. - Channel to chamber connection was compromised causing pressure buildup.	- Port indicators were removed. - Ports were extended into the chamber.
3	- Facilitated glass slide addition. - Ports inside the chamber would provide easier connection of channel to chamber and reduce pressure buildup.		- Ports extended inside the chamber reduced pressure buildup of liquid, but connection of channel to port was still compromised.	- Conical features were added to the ports inside the chamber to increase surface area at the point of channel-chamber connection.
4	- Facilitated glass slide addition. - Conical features on ports provided more surface area to connect printed channel to chamber.		- Chamber length only permitted printing of channels 15mm in length.	- Length of chamber was increased to 25mm.
5	- Facilitated glass slide addition. - Conical features provided excellent connection of channel to chamber.		-	-

The first design made lining up the print head to the hole of the port very difficult. Channels printed using this chamber were crooked and did not line up perfectly with the

channel ports. The bottom of the chamber was very snug around the microscope slide making inserting the slide somewhat dangerous. Multiple microscope slides were broken when trying to add them to the chamber. To resolve these issues, the chamber was modified. The width of the bottom of the chamber was increased by 2mm, and the projections were shortened and beveled to ensure easier addition of the microscope slide. Additionally, features were added above each channel port to indicate where the port was located.

This modification allowed for easier and safer addition of microscope slides to the bottom of the chamber. However, the features above the ports did not work properly. The projections interfered with the nozzle while printing. Therefore, they were removed. However, additional issues with the design were encountered. The printed channels would not connect to the chamber ports. Even if channels were lined up perfectly with the ports, the design did not facilitate connection between the print and the ports. When flushing channels with water, the fluid would build up between the solidified matrix phase and the wall of the chamber when flushing the channels, eventually diverting upwards and pooling on the top of the matrix phase as shown in Figure 11.

Figure 11: Optimization of the printing chamber geometry. The red syringe tip is inserted into the left side of the channel pushing water from left to right. Fluid buildup on the right side of the channel caused pooling of liquid on the surface of the matrix phase.

To circumvent these issues, ports were extended into the chamber to reduce pressure build up and facilitate lining up the printed channels with the ports. This modification reduced pressure buildup, but the printed channels still had poor connections to the chamber. To combat this issue, conical features were added to increase surface area at the point of connection between printed channel and chamber. Gelling and crosslinking of the matrix phase around the conical features would also reduce the probability of the matrix phase detaching from the chamber and diverting fluid. These modifications resolved the issues surrounding pressure buildup and provided easier connection of the printed channel to the ports of the chamber. However, the length of the channels were limited by the length of the chamber. The Thorlabs motors used for printing have a maximum range of 25 mm. Therefore, the length of the printing chamber was increased to 25 mm between the channel ports. Figure 12 displays the final design for the printing chamber. Dimensions of the chamber are displayed in the engineering drawing (see Appendix A: Supplementary Figures; Figure A1).

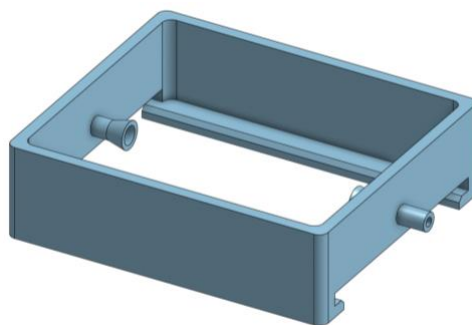Figure 12: The final version of the printing chamber designed using Onshape. This chamber is used for RL3DP of microchannels with the ink and matrix phase. The design of this chamber allows for addition of a microscope slide after printing to allow for microscopic visualization of the printed channels. The conical ports on both ends of the chamber allow for channel connection for perfusion of media.

3.1.1.1 3D Printing of the Channel Printing Chamber

The printing chamber was designed using Onshape, an online CAD software. Once the design was finalized, the part was exported in binary STL format and uploaded to a third-party slicing software called ChiTuBox to prepare the file for printing. The bottom of the chamber has a large region of overhang where the microscope slide attachment resides. To eliminate the need for supports in this region, and to ensure the chamber printed properly, the chamber was printed upside down. To ensure the ports on either side of the chamber form properly, supports were added underneath each port on the inside and outside on as shown in Figure 13. Print settings were adjusted (see Appendix B; Table B1), the chamber was sliced into 10,000 layers and saved on a USB as a CTB file.
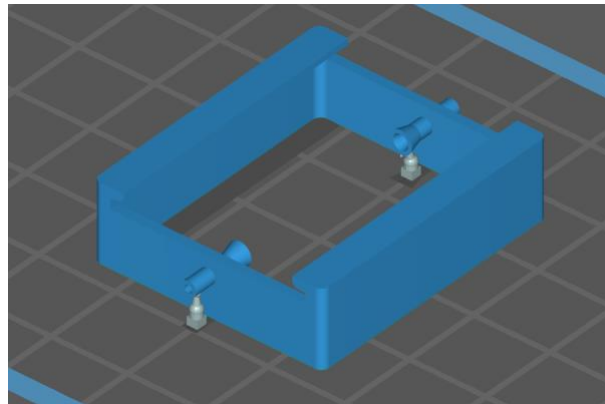
Figure 13: Preparation of the printing chamber file in ChiTuBox software. The chamber was flipped upside down on the build plate and supports were added under each port feature.

The USB drive containing the print file was inserted in the ELEGOO Mars 2.0 UV Photocuring 3D printer. Before the print began, UV-curing standard photopolymer resin was added to the tray, and the build plate was cleaned and screwed securely to the printer. The printing chamber took approximately 40 minutes to print. Once finished, the build plate was unscrewed, and an attachment was used to tilt the build tray so excess resin dripped off. A razor and putty knife were then used to carefully remove the printing chamber from

the build plate without damage. The razor blade was used to slide along the build plate under each corner of the printing chamber to separate it from the build plate. The putty knife was used to wedge under the razor blade and slowly lift the chamber until it was removed from the build plate. The razor blade was used to carefully remove the four supports placed on the channel ports. The printing chamber was then washed in a 70% isopropyl alcohol bath to remove any uncured resin, dried using pressurized air, and cured for 5 minutes on each side using the ELEGOO Mercury Curing Machine. The printing chamber was finalized by adding the microscope slide through the slots on the bottom of the chamber and sealed along the edges using hot glue to prevent leaking as shown in Figure 14.

Figure 14: The printing chamber with a clear microscope slide attached. The microscope slide is hot glued in place to prevent leaking.

3.1.2 Rapid Liquid 3D Printing Setup

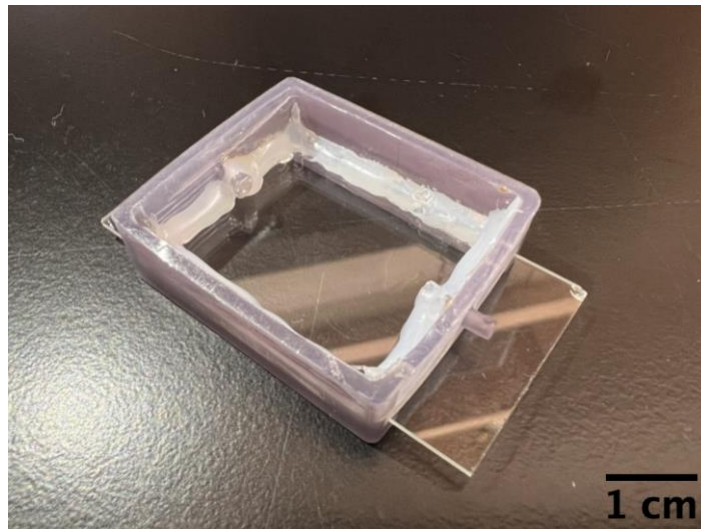To build the RL3DP system, three 25mm MTS25-Z8 motorized translation stages were purchased from Thorlabs and arranged in an x-y-z configuration for printing. Each translation stage was controlled by a DC servo motor and movements were programmed

using the Kinesis software on an external computer. An attachment serving as the Thorlabs printhead was designed in Onshape and printed on the ELEGOO Mars 2.0 UV Photocuring 3D printer using similar procedures to those described for the printing chamber. An external KD Scientific LEGATO syringe pump was used to control the volumetric flow rate of the ink phase. A 3 mL BD Luer lock syringe with a 13-gauge syringe tip attached to 2.5 mm diameter tubing connected the syringe to the print head mounted on the Thorlabs printer. The nozzle used for printing was a modified Luer lock syringe tip with one end attached to the tubing and the Luer lock attached to a 25-gauge syringe tip with inner and outer diameters of 0.25 and 0.5 mm, respectively. The complete RL3DP setup is displayed in Figure 15.
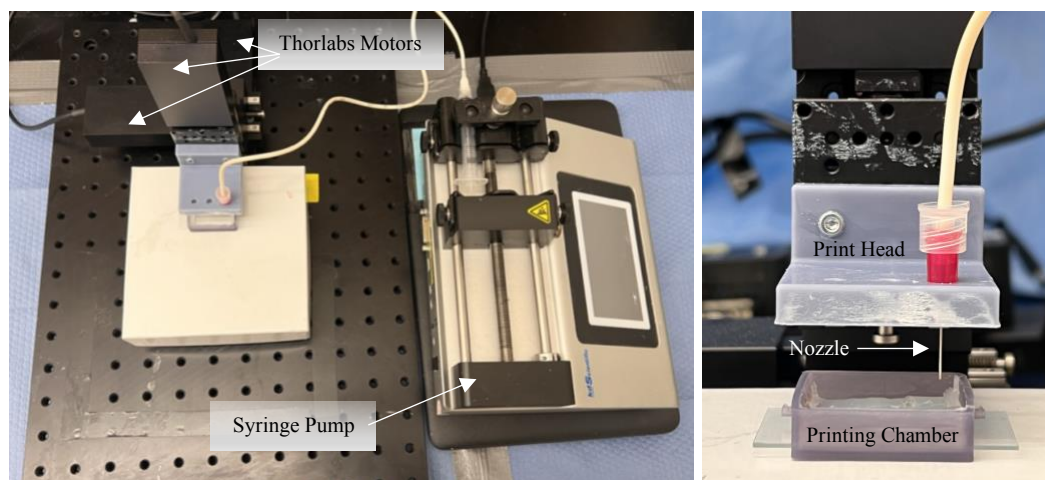
Figure 15: The RL3DP printing system. (Left) The x-y-z configuration of the Thorlabs MTS25-Z8 motorized translation stages and the external KD scientific LEGATO syringe pump with syringe and tubing attached. (Right) A closer image of the print head showing the 3D printed attachment to hold the modified nozzle. Also pictured is the printing chamber used to house the matrix phase while printing.

3.1.3 Rapid Liquid 3D Printing Process

Polymers used for printing were prepared using the process outlined in 2.1.2.1. Polymer solutions for the ink and matrix phase were made 24 hours in advance and stored at 4°C.

Thirty minutes before printing, the Falcon tube containing matrix phase was placed in a water bath at 40°C and the Falcon tube containing ink phase was left at room temperature on a shaker plate. The matrix phase was kept at 40°C to prevent premature gelling of the matrix phase as it cooled during printing. The ink phase remained at room temperature as the ink could not be kept warm during printing with the setup used for this project. Once the matrix phase became liquid, it was centrifuged for 2 minutes at 1400 RCF to remove any air bubbles present in the liquid and was then placed back into the 40°C water bath. Once the ink reached room temperature, a 3mL Luer lock BD syringe with a 13-gauge syringe tip was used to collect 3mL of the ink phase. The syringe tip was inserted into the 2.5 mm diameter tubing connected to the print head. The plunger was pushed until ink filled the entire length of tubing and dripped from the nozzle. The syringe pump was turned on and the syringe containing ink with attached tubing was secured to the syringe pump. The desired flow rate was chosen on the syringe pump and left to run for 5 minutes before a print to ensure no pressure buildup of fluid and the volumetric flow rate of ink had equilibrized. During that time, the Thorlabs motors were powered on and connected to the external computer containing the Kinesis software. Within the software, the three Thorlabs motors were loaded and set to their home position. Before a print, the desired distance, acceleration, and translation speed were set for each motor. When ready to print, the matrix phase was removed from the water bath and ~3.0 mL of matrix phase was poured into an empty printing chamber to cover the channel ports without overflowing the rim of the chamber. Two pins were inserted into the ports of the printing chamber to facilitate connection of the channel to the chamber after printing. The printing chamber containing matrix phase and pins was transferred over to the printing stage and the port was lined up vertically with the nozzle head. The Kinesis software was used to lower the nozzle so that

the print tip was extruding ink directly beside one port with a needle in place. The nozzle was left in this position for 5-10 seconds, depending on the volumetric flow rate of ink, to create a droplet beside the port to facilitate connection of the channel to the port later. The x-axis motor was used to move the print head through the matrix phase forming a channel from left to right. The nozzle was left to continue extruding ink at the opposite channel port for another 5-10 seconds before it was lifted by the z-axis motor and moved away from the printing chamber. When removing the pins, the droplet of ink surrounding the pin was pulled directly through the channel ports, establishing the connection between the channel and the chamber. The printing chamber was left to rest untouched at room temperature for 30 minutes to ensure the matrix phase had completely gelled. Once gelled, 2 mL of 0.1 M CaCl$_2$ was placed on top of the gelled matrix phase. After 20 minutes, the crosslinker was removed and 2 mL of DMEM/F-12 was added to the top of the matrix phase to reduce evaporation of the matrix phase. A 3 mL BD syringe loaded with DMEM/F-12 and a 13-gauge syringe tip was used to slowly flush out the ink in the channel at 0.1 ul/min leaving behind a hollow microchannel.

3.1.4   Channel Imaging

A Nikon Eclipse Ti Epifluorescence microscope was used to image the printed channels. Single frame images at 2X magnification did not capture the entire length of the channel. However, the software allowed image stitching of multiple images together to create a single high-resolution mosaic image. This setting was used to produce a single image that captured the entire length of the channel. However, brightfield images captured microbubbles in the surrounding matrix making it difficult to analyze channel dimensions.

To better highlight the channel boundaries, 0.01% FITC-Dextran was flowed through the channels and imaged using fluorescence microscopy.

3.2 Experimental Results and Discussion

3.2.1 Hollow Microchannels in Crosslinked Hydrogel Network

Hundreds of channels were printed and imaged over the course of this project. The following images highlight only a few channels to demonstrate the overall result of the RL3DP process. All channels were printed from left to right.
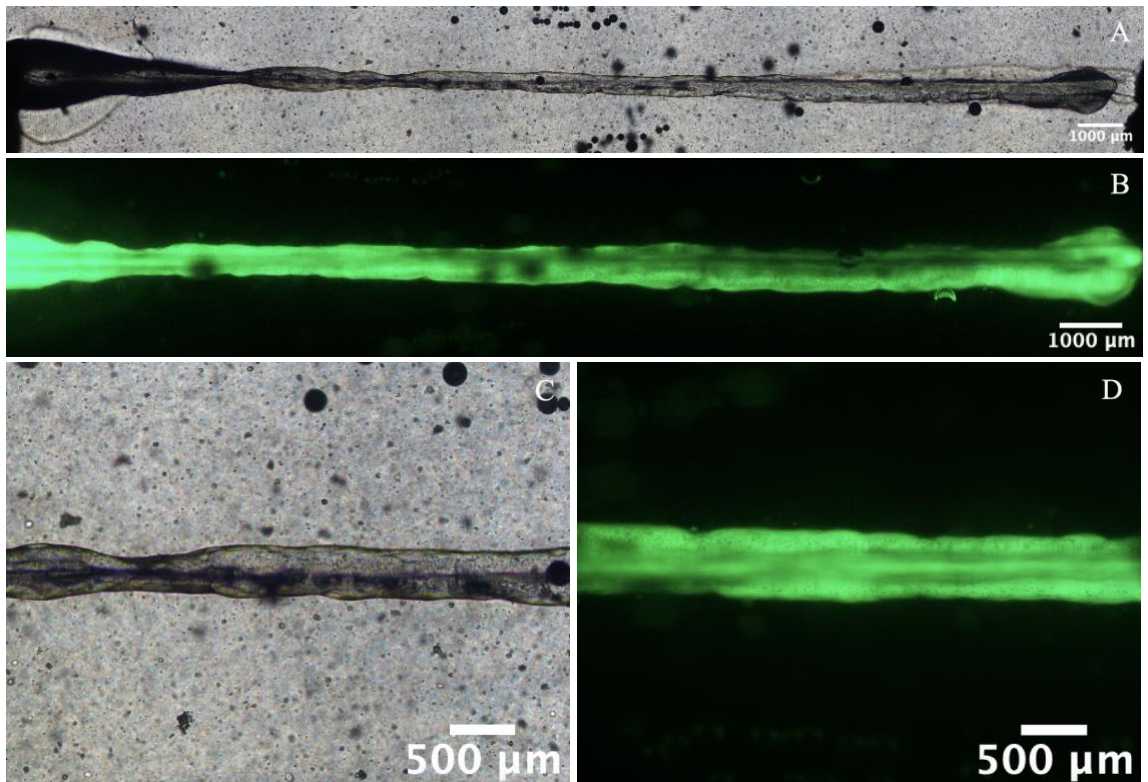
Figure 16: Brightfield and fluorescence images of a channel printed with a translation speed of 0.4 mm/s and a volumetric flow rate of 20 µl/min. A) Brightfield and B) fluorescence mosaic images of the entire channel length captured at 2X magnification. C) Brightfield and D) fluorescence images of the middle segment of the printed channel at 2X magnification. The diameter of the channel is roughly 350-400 µm.
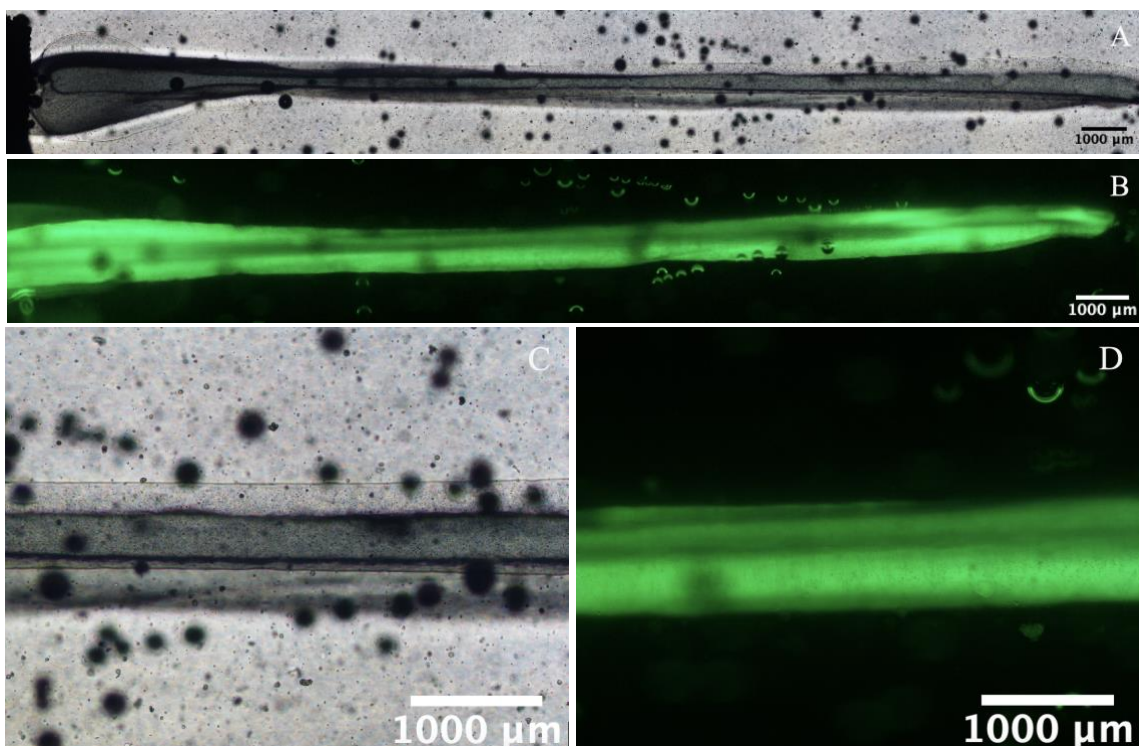
Figure 17: Brightfield and fluorescence images of a channel printed with a translation speed of 0.2 mm/s and a volumetric flow rate of 25 μl/min. A) Brightfield and B) fluorescence mosaic images of the entire channel length at 2X magnification. C) Brightfield and D) fluorescence images of the middle segment of the printed channel at 2X magnification. The diameter of the channel is roughly 650-700 μm.

Figure 16 displays brightfield and fluorescence images of a channel printed with a translation speed of 0.4 mm/s and a volumetric flow rate of 20 ul/min resulting in a channel diameter of ~350 μm. Figure 17 displays brightfield and fluorescence images of a channel printed with a translation speed of 0.2 mm/s and a volumetric flow rate of 25 ul/min resulting in a channel diameter of ~650 μm. These channels are considered uniform as they maintain roughly the same diameter along the entire length of the channel.

3.2.2 Achievable Channel Diameters

The diameter of a printed channel depends on the volumetric flow rate of ink and the translation speed of the print head. Therefore, a wide range of diameters are achievable by

manipulating both translation speed and volumetric flow rate. Increasing translation speed and decreasing volumetric flow rate results in smaller channel diameters. Conversely, decreasing translation speed and increasing volumetric flow rate produces channels with substantially larger diameters. Figure 18 displays the relationship between translation speed of the print head and the resulting channel diameter for different volumetric flow rates of ink. Triplicate experiments were performed to ensure repeatability of the printing process.
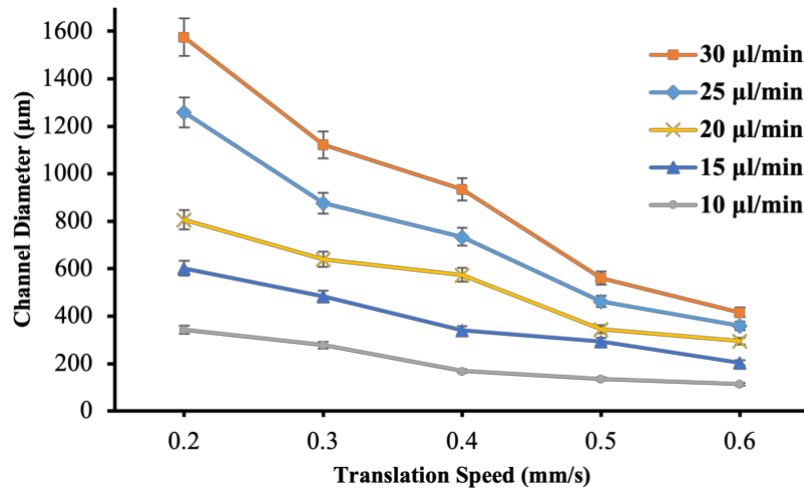
Figure 18: Graph of translation speed vs. channel diameter for different volumetric flow rates of ink that produced uniform microchannels. N=3 for each volumetric flow rate of ink.

Between volumetric flow rates of 10-30 μl/min, channel diameters ranging from 100-1500 μm were achievable. Repeatability of the printing process was achieved, channel diameters printed with the same volumetric flow rate of ink and translation speed of the print head produced channels with roughly the same diameter (± 10μm). Lower translation speeds had higher variability due to the higher volume of ink deposited. It was possible to print larger diameter channels with higher volumetric flow rates of the ink. However, the diameters of these channels would be beyond the range appropriate for microvasculature research.

3.2.3 Channel Uniformity and Complexity

An important aspect of this project was to ensure repeatability of the printing process. Experiments with the same translation speed and volumetric flow rate settings should produce channels with similar diameter and uniformity. It is inevitable that the beginning and end of a print is somewhat non-uniform because the ink is left to build up forming a droplet of ink which connects the channel to the ports. Additionally, there is a transition period between the droplet and where the channel begins forming properly of around 1-5 mm depending on speed and flow rate of ink. Any further applications using RL3DP must incorporate the initial transition period of printing into the final design.

There exists an optimal range of printing that produces uniform channels which maintain their form. Slower translation speeds generally result in more uniform channels that maintain the same diameter along the entire length of the channel. However, channels printed at higher translation speeds tend to be non-uniform. Figure 19 displays two channels printed with the exact same volumetric flow rate of ink but different translation speeds.
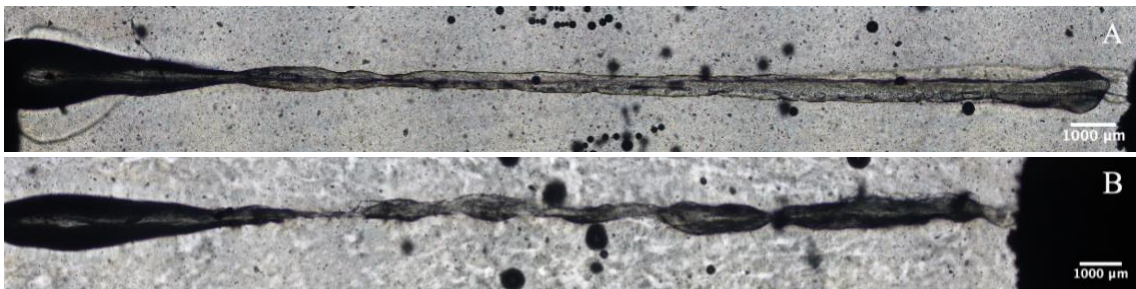
Figure 19: The result of printing a channel at A) low and B) high translation speeds. The channels were printed with a volumetric flow rate of 20 μl/min and a translation speed of A) 0.4 mm/s and B) 0.7 mm/s.

Channel A was printed at 0.4 mm/s and channel B was printed at 0.7 mm/s. The first channel maintained a uniform shape along the entire length of the channel whereas the second channel was less uniform. This phenomenon was observed at translation speeds

above 0.6 mm/s for every volumetric flow rate. Higher translation speeds may have increased turbulence in the matrix phase causing eddies to form behind the print head. As displayed in Figure 20, formation of eddies may have caused the matrix phase to swirl behind the nozzle displacing the ink during printing, creating a non-uniform channel with periodic "bubbles" of ink.
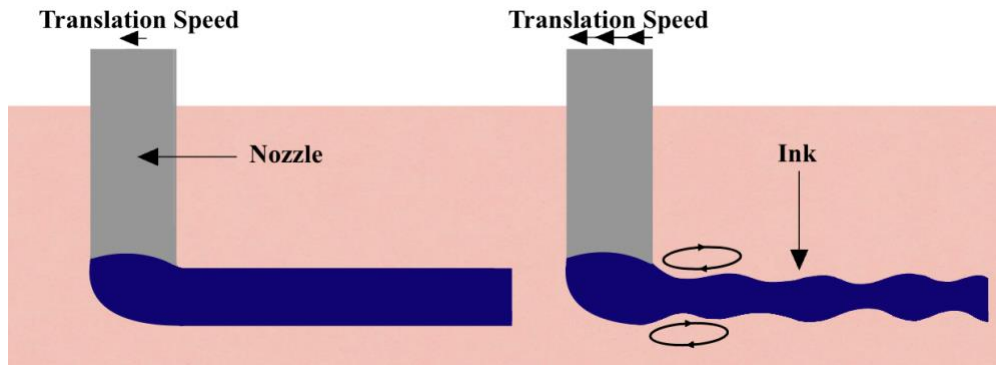
Figure 20: Schematic depicting the formation of channels at (left) slower translation speeds and (right) faster translation speeds. The pink and white regions indicate the matrix-air interface, respectively. The blue ink is extruding out of the grey nozzle. Increasing the translation speed of the print head may increase turbulence in the matrix phase, which may cause eddies to form behind the printing nozzle forming non-uniform channels.

The optimal range of printing determined from these experiments were translation speeds between 0.2-0.6 mm/s. Translation speeds of 0.7 mm/s and above formed non uniform channels. However, there is not a very strict optimal range for printing for the volumetric flow rate of ink. Higher volumetric flow rates of ink result in larger channel diameters. However, lower volumetric flow rates must be printed at lower translation speeds because enough ink must be extruded to form a channel properly. Therefore, only volumetric flow rates of 10 μl/min and above were tested to avoid this issue.

This thesis focused on printing straight-line channels from one chamber port to another. However, future work in RL3DP for tissue modelling applications will print complex

channel designs that resemble native vascular networks. Although the project was not able to reach that stage of complexity, some preliminary testing of printing more complex designs was tested. The goal of this experiment was to analyze if a channel could be printed perpendicularly off a previously printed channel and if those channels were interconnected. The first channel was printed in a straight line from left to right in the x-plane. The second channel was printed perpendicularly from the middle of the first channel. As shown in Figure 21, printing of the second channel dragged the first channel through the matrix phase along with it.

Figure 21: The result of an experiment where a channel was printed perpendicularly off a previously printed channel.

After solidifying the matrix phase, the ink was flushed out resulting in two interconnected channels. Water was easily flushed through both printed channels, meaning this technique could be used to connect channels together creating a network of hollow microchannels inside a hydrogel matrix. However, movement of the first channel throughout the matrix phase during printing is detrimental to print fidelity. When printing

more complex designs with multiple interconnected channels, the ink would have to remain where it is deposited. Potential solutions include printing at slower translation speeds or increasing the viscosity of the ink and/or matrix phase and to reduce the probability of movement during printing.

3.3 Chapter Summary

Using RL3DP techniques, the ATPS formulation created for this project was capable of producing uniform hollow microchannels within a hydrogel matrix. Microchannels of various dimensions were created by adjusting the volumetric flow rate of the ink and the translation speed of the print head. The RL3DP setup used for this project was capable of producing channels ranging from 100-1500 μm in diameter. Stabilization of the hydrogel matrix by gelation and crosslinking allowed for removal of the ink phase leaving a hollow microchannel behind. The printing chamber designed for this application allowed for microscopic visualization of the printed channels. This feature allowed for high resolution imaging to analyze channel uniformity. Additionally, the chamber ports provided a means of attaching the chamber to a pulsatile pump for cell culture applications.

Chapter 4: Physical and Biological Properties of Ink and Matrix Phase

This chapter focuses on analyzing characteristics of the ink and matrix phase formulations used in the design of a system used for rapid liquid 3D printing (RL3DP). Rheology of the ink and matrix phase define how the material responds to deformation and identifies how the viscosity, storage modulus, and loss modulus of the material changes with temperature. Mass loss and compression testing experiments were performed on the matrix phase to understand the degradation rates and compressive modulus of the material.

4.1 Materials and Methodology

4.1.1 Rheometry

Rheological properties such as viscosity, storage modulus, and loss modulus quantify how a material responds to external forces. The field of 3D bioprinting relies heavily on the specific viscosity of materials to ensure proper shape fidelity and print stability. In the field of RL3DP, the matrix phase is exposed to shear stress throughout the process of printing. Additionally, the ink phase must be shear-thinning as it is forced through tubing until being deposited in the matrix phase where it is exposed to the surrounding medium. Therefore, rheological properties of both the ink and matrix phase are of interest for RL3DP to quantify how each material responds to such forces.

The HR 10 Discovery Hybrid Rheometer with the 40.0 mm 2.00083° advanced Peltier cone and plate attachment was used for rheometry experiments. Polymer solutions were prepared using the process outlined in section 2.1.2.1. To begin the experiments, the rheometer was turned on, the air pressure valve opened, and the coolant tank was filled. The computer attached to the rheometer was then powered on and the TRIOS software was

loaded. This software was used to control the rheometer movements, setup experiments, and record data. To load the polymer solutions, the software was used to raise the top plate to the loading gap and 200 µl of solution was placed directly in the middle of the plate. When loaded, the plate was set to a gap of 0.02µm between the top and bottom plates as directed by the software. Excess polymer was removed around the cone plate with a Kim wipe. Figure 22 displays the final setup before testing.

Figure 22: The HR 10 Discovery Hybrid Rheometer with cone and plate attachment. The device below the testing area is a warming plate used to control the temperature during the experiment.

An oscillation temperature ramp experiment was used to measure the complex viscosity, storage modulus, and loss modulus of both the ink and uncrosslinked matrix phase over a temperature ramp of 10-40°C. The test parameters for these experiments were a 1% strain rate, temperature ramp rate of 1.0 °C/min, and an equilibration time of 60 seconds to ensure the polymer reached the desired temperature. Data points were collected every 3 seconds during the experiment. At the end of an experiment, the top plate was raised, and all pieces

were removed to clean off the polymer solution. Data points were collected using the TRIOS software and exported into an Excel file after each experiment

4.1.2 Degradation of Mass

The constructs created using this RL3DP system are intended to be used for soft tissue modeling and the matrix phase will be exposed to cell culture conditions for upwards of 2-4 weeks depending on the specific application. Therefore, the matrix phase will be expected to degrade overtime. To ensure the matrix phase is suitable for such applications, it is very important to analyze the rate and degree of degradation (i.e. mass loss).

Mass loss of the matrix phase was determined by drying and weighing samples over a period of 12 days. Experiments were run in triplicate. The experimental setup involved preparing three sets of sterile crosslinked cylindrical polymer specimens using the process outlined in section 2.1.2.3. Since the experiment was held over a 2-week period, there was a high risk of contamination. Experiments were performed inside the BSC, and all materials were properly sanitized.

Each day, three 60 mm cell culture dishes were marked with the date and experiment number and weighed on the balance. The initial weight of the dish was recorded because these dishes would house the specimens as they dried. The initial weight was subtracted from the total weight to find the final mass of polymer after drying. Once weighed and marked, the dishes were sprayed with 70% ethanol and placed inside the BSC. The three 12-well plates were removed from the incubator and placed inside the BSC. One specimen was removed from each of the three plates using a micro spatula tool and placed in the corresponding dish. The media was removed from each well and fresh sterile DMEM/F-12 with 1% antibiotic was placed back on the remaining specimens and the plates were put

back in the incubator. The three culture dishes containing the specimens were removed from the BSC and RO water was added to the dish. The specimens were rinsed on a shaker plate for one minute to remove media and salts on the outside of the specimens. The water was removed, and dishes were placed in a dry oven set to 37 °C. The mass of the drying sample was measured daily until there was no further decrease in mass and all the moisture had been removed from the sample. The final dry weight was calculated by subtracting the initial mass of the dish by the final mass of the dish containing the dried polymer specimen. Once all 12 samples were processed and dried, the percent mass loss for each day was calculated using Eq. 1 where M_i is the calculated initial mass of dry polymer in each specimen and M_f is the final mass recorded after approximately 96 hours of drying.

$$Percent\ Mass\ Loss = \frac{M_i - M_f}{M_i} * 100 \qquad \text{Eq. 1}$$

4.1.3 Compression Testing

Tissue models used to culture cells are exposed to various types of internal and external forces throughout the process of culturing. Models are constantly being manipulated for research purposes and cells impart forces on their surroundings when growing, proliferating, and migrating. Additionally, stiffness of cell culture substrates directly impacts cellular function through mechanotransduction (Parker & Ingber, 2007). Therefore, it is important to understand the mechanical properties of the matrix phase.

Mechanical strength of the crosslinked matrix phase was analyzed using a Mark-10 F105 motorized force tester machine. Experiments were run in triplicate. The experimental setup involved preparing three sets of sterile crosslinked cylindrical polymer specimens using the process outlined in section 2.1.2.3. Since the experiment was held over a 2-week period,

there was a high risk of contamination. Experiments were performed inside the BSC, and all materials were properly sanitized.

The Mark-10 motorized force tester was equipped with a 10N load cell attached to a 50 mm diameter plate which compressed down onto the sample sitting on a 3D printed 50 mm diameter plate. To avoid slipping while testing, a piece of paper towel was placed under the sample and the samples were patted dry before testing. The Mark-10 machine was connected to a tablet equipped with intelliMESUR Gauge software used to program and control the machine as well as collect data. For the compression tests, the Break Limit test setting was used which identifies a break in the material when the load drops by a specified percentage. The basic setup of the break limit test was a break threshold of 0.15N, a break percentage drop of 50%, and a compression speed of 0.1 mm/s. To begin an experiment, the top plate was controlled using the software and carefully positioned to measure the initial height of the sample as shown on the left in Figure 23. The force and distance were tared to zero. Once the experiment began, the samples were compressed until a break had occurred and the software stopped gathering data, as shown on the right in Figure 23.
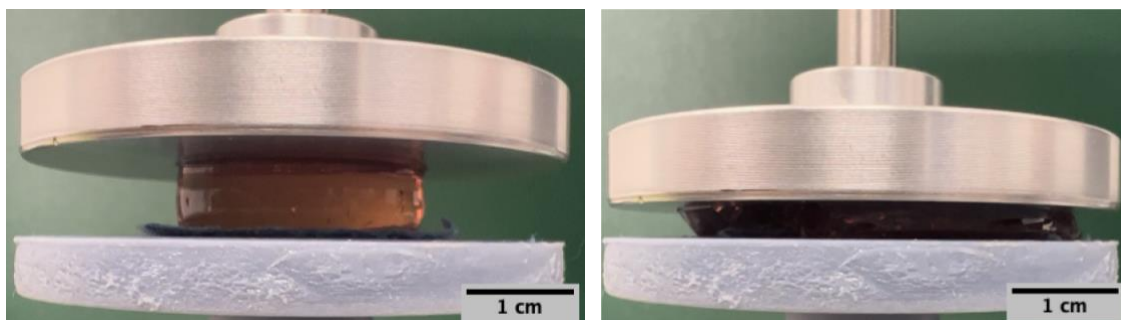

Figure 23: The setup for compression testing experiments. (Left) The sample on the compression plate before the test began. (Right) The end of a sample run where a break was detected in the sample.

Once the experiment was completed, the top plate was raised, and the fractured sample was removed. The software reported force-displacement graphs and tables for each experiment which were converted to stress-strain curves to determine the compressive elastic modulus of each sample.

4.1.4 Cell Viability Assay

The constructs created using this RL3DP system are intended to be used to culture cells for soft tissue modeling. The polymer used in the matrix phase must not have any adverse effects on cultured cells. Therefore, it is important to assess cell viability when cells are cultured in the matrix phase. Experiments were run in triplicate. The cells used to assess cell viability of the matrix phase were Lund human mesencephalic embryonic stem (LUHMES) cells. These cells are from human origin and are neuronal precursor cells (Edwards & Bloom, 2019). The main goal of the assays was to measure cell viability when the cells were evenly distributed throughout the matrix phase. Instead of culturing cells on top of the matrix phase, the cells were mixed into the matrix phase meaning cells were cultured in a 3D environment. Viability assays must penetrate through the matrix phase and into the cells in order to accurately access the viability of cultured cells. Therefore, a 3-(4,5-dimethylthiazol-2-yl)-2,5-diphenyltetra- zoliumbromide (MTT, Sigma-Aldrich) assay was used to measure cellular metabolic activity, which indicates cell viability, proliferation, and cytotoxicity of materials (Legna, 1988). The MTT reagent is reduced to purple formazan crystals in living cells which can later be measured by absorbance.

LUHMES cells (LUHMES; CRL-2927, ATCC) were cultured according to established protocols (Zang, Yin, & Zhang, 2014; Edwards & Bloom, 2019). Cells were cultured in vented 75 cm^2 flasks incubated in a humid atmosphere at 37 °C in 5% CO_2. Cell culture

flasks were pre-coated with 50 ug/mL poly-L-ornithine (Sigma) overnight at room temperature followed by 1 ug/mL human plasma fibronectin (Sigma) overnight at 37 °C, rinsed with phosphate-buffered saline (PBS), and allowed to fully air dry before cell plating. LUHMES cells were cultured in Dulbecco's Modified Eagle Medium F12 (DMEM F12) (Corning) supplemented with 1X N2 supplement (TMO) and 40 ng/mL human recombinant basic FGF (Sigma) added fresh right before media changes. Cells were used before passage number 20 and subcultured when flasks reached 80% confluency.

To prepare cells for the MTT assay, embryoid bodies were made by seeding cells onto non-coated 12-well cell culture plates. Low attachment cell culture plates cause cells to aggregate together naturally forming 3D spheroids. Embryoid bodies were used in this study as baseline LUHMES cell viability was greater in this format. When subculturing a plate of cells, cells were seeded into each well of a non-coated 12-well plate at a seeding density of 6.7×10^5 and cultured in 0.5mL of their respective media in a humidified incubator at 37 °C with 5% CO_2. After 24 hours of culturing, each well was topped up with 0.5 mL of supplemented media and the bottom of each well was gently scraped with a pipette tip to re-suspend the cells. To change the media after 48 hours of culturing, the 12-well plate was tilted and left for ~5 minutes to ensure all embryoid bodies sank to the bottom side of the well. Media was aspirated ensuring no embryoid bodies were removed from each well and replenished with 1.0mL of supplemented media. Embryoid bodies were cultured for 4-5 days before harvesting.

The experimental setup for the MTT assays involved preparing 20 mL of sterile matrix phase following the process outlined in section 2.1.2.2 which was kept in a water bath at 37 °C. Embryoid bodies were harvested and filtered through a 100 µm pore size cell strainer to collect embryoid bodies of 100 µm in diameter or larger. Embryoid bodies were collected

and carefully mixed into 20 mL of sterile matrix phase. The Falcon tube containing embryoid body infused matrix phase was mixed by inversion to reduce the amount of sheer stress on the embryoid bodies and the suspension was transferred to a 20 mL BD syringe. This syringe was used to deposit 1.0 mL of cell seeded matrix phase into 9 wells of a 12-well plate. The remining 3 wells were used as controls and seeded with $4x10^5$ LUHMES cells directly on the tissue culture plastic without any matrix phase present. The plate was left to sit at room temperature for 30 minutes to allow for gelling of the matrix phase. The wells containing cell-seeded matrix phase were crosslinked using 1.0 mL of 0.1 M $CaCl_2$ and left for 20 minutes. The crosslinker was removed and the cylindrical crosslinked cell-seeded matrix phase specimens were cultured in 1.0 mL of their respective media in a humidified incubator at 37 °C with 5% CO_2.

At 24 and 48 hours of culture, a plate was removed from the incubator and placed inside the BSC. The methods for the MTT assays were modified to account for penetration time into the hydrogel matrix. MTT reagent (5mg/mL) and fresh supplemented media were mixed together in a Falcon tube at a 1:1 ratio and 1.0 mL was added to each well of the plate and cultured overnight in a humidified incubator at 37 °C with 5% CO_2. The MTT/media solution was aspirated and replaced with 1.0 mL of dimethyl sulfoxide (DMSO) and left in a dark environment on a shaker plate for 2 hours at room temperature. The DMSO solution dissolves the formazan crystals out of the matrix phase and into solution. Optical density of the formazan solution from each well was measured at 570 nm using a FilterMax F5 plate reader. A one-way analysis of variance (ANOVA) test using SPSS software was performed to determine statistical significance between conditions.

4.2 Experimental Results and Discussion

4.2.1 Rheometry

Rheology tests were performed to understand the complex viscosity, storage modulus and loss modulus of the system change with respect to temperature. Figure 24 displays the results for complex viscosity vs. temperature for both the ink and matrix phases.
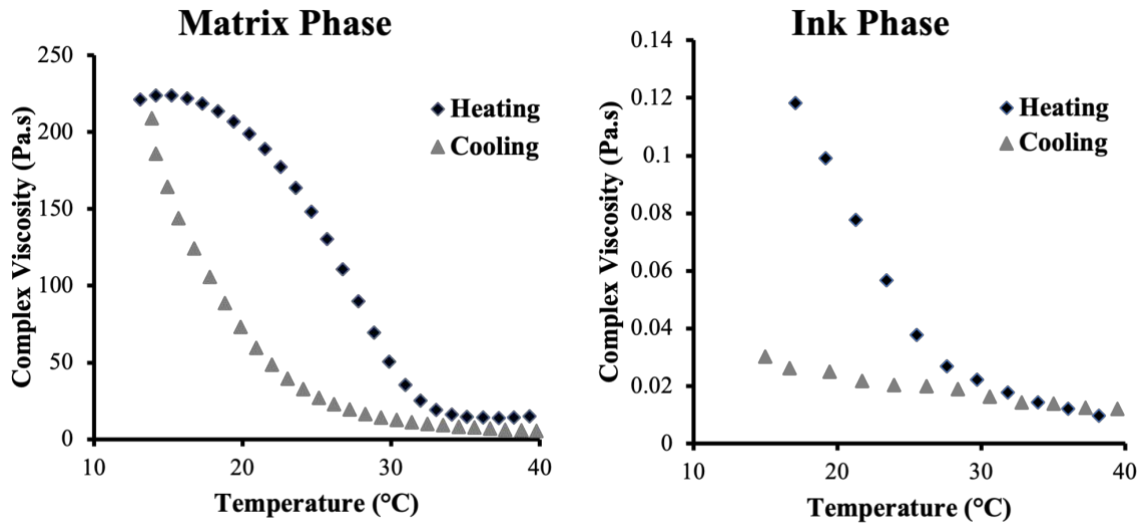

Figure 24: Complex viscosity vs. temperature results for (left) matrix phase and (right) ink phase between 10-40 °C. The blue diamond markers indicate the results from heating the polymer solution and the grey triangle markers indicate the results from cooling the polymer solution. This is for a single trial experiment.

Viscosity is inversely proportional to temperature (Hossain, Munir, & Pop, 2001). As temperature increases, the viscosity of the polymer will decrease and vice versa. However, the rate at which viscosity changes with respect to temperature depends on whether the polymer is being heated or cooled. For example, the matrix phase has a viscosity of 210 Pa·s and 60 Pa·s at 20 °C during the heating and cooling process, respectively. At 15 °C, the matrix phase is fully gelled and therefore has a high viscosity. As the polymer blend is heated, the polymer strands are slowly transitioning to a more disordered arrangement. This

is described as the melting temperature. Conversely, at 35 °C, the matrix phase is fully liquified and therefore has a much lower viscosity. As the polymer blend is being cooled, the polymer strands are slowly transitioning into a more ordered state. This is described as the gelling temperature. Therefore, the difference in magnitude of viscosity values as the matrix phase is being heated or cooled is dependent on the initial state of the polymer blend.

Compared to the matrix phase, the viscosity vs. temperature results for the ink phase are noticeably different. Although the data appears similar to the matrix phase, the difference in magnitude between heating and cooling is much lower. The largest difference is only 0.1 Pa·s, meaning that the viscosity of the ink phase does not change considerably with temperature. For extrusion-based 3D bioprinting applications where an ink is used to 3D print a tissue model, high viscosity inks are more commonly used to increase shape fidelity and print stability (Becker, Gurian, Schot, & Jeroen, 2022). However, for the application of RL3DP, the opposite is true. RL3DP requires a highly viscous or granular-like medium that supports the ink while printing. Therefore, the ink phase can have a relatively low viscosity compared to the matrix. However, for this project, the viscosity of the ink phase is remarkably lower than the viscosity of the matrix phase. At 37°C, the complex viscosity for the matrix phase and ink phase are 13.87 and 0.012 Pa.s, respectively. Although this combination of polymers creates uniform microchannels, increasing the viscosity of the ink phase would most likely improve shape fidelity and print stability.

In addition to viscosity, an important characteristic of the matrix phase is the storage and loss modulus of the polymer blend. Storage and loss modulus values identify the materials ability to store elastic energy. Figure 25 displays the results for storage and loss modulus vs. temperature for the matrix phase.
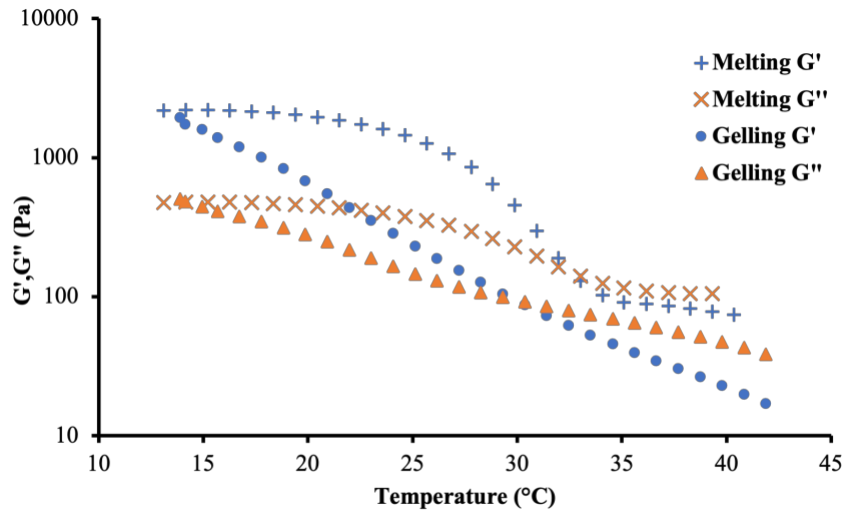
Figure 25: Storage Modulus (G') and Loss Modulus (G") vs. temperature for the matrix phase between 15-40 °C. The blue cross and circle markers indicate the storage modulus results for melting and gelling experiments, respectively. The orange x and triangle markers indicate the loss modulus results for melting and gelling experiments, respectively. This is for a single trial experiment.

The modulus of a material represents the magnitude of resistance to deformation. The storage and loss modulus gradually decrease as the temperature increases due to the higher mobility of polymer chains as temperature increases. The sol-gel transition temperature, otherwise called the melting temperature (T_m), and the gel-sol transition temperature, otherwise known as the gelation temperature (T_g) is obtained from where G' and G" intersect during the heating and cooling process, respectively (Osorio, Bilbao, Bustos, & Alvarez, 2007). Here, T_g and T_m are equal to 29 and 33°C, respectively. Furthermore, the relaxation observed in both the storage and loss modulus during the melting experiment around 33°C indicates the sol-gel transition temperature. For this application, the printing process takes place around 37°C and is then left to cool on the bench top after printing. A gelation and melting temperature of 29 and 33°C respectively is excellent for this

application as the matrix phase remains a liquid when printing and will gel when left at room temperature.

4.2.2   Degradation of Mass

This polymer combination will be used to create tissue models through the process of RL3DP. The resulting model will incorporate cells and be exposed to cell culture conditions for up to 2-4 weeks depending on the application. Therefore, it is very important to analyze how the matrix phase degrades over time and to record the magnitude of that degradation by way of mass loss. Figure 26 displays the results for percent mass loss versus time for the matrix phase combination.

Figure 26: Percent mass loss versus time in days for the matrix phase combination of 5 wt.% gelatin, 2 wt.% alginate crosslinked with 0.1 M $CaCl_2$ and 20 wt.% Sucrose. Experiments were run in triplicate to validate results, N=3.

There is an initial mass loss of 50% after just 1 day of incubation which continuously increases until day 5-6 where it begins to plateau around 90% mass loss. At first glance, these values for mass loss may be reason for concern. However, over the 12-day period, the cylindrical specimens maintained their shape very well and were able to be transferred

and manipulated without falling apart or losing their structure. Figure 27 displays a picture of a matrix phase specimen after 12 days of degradation.
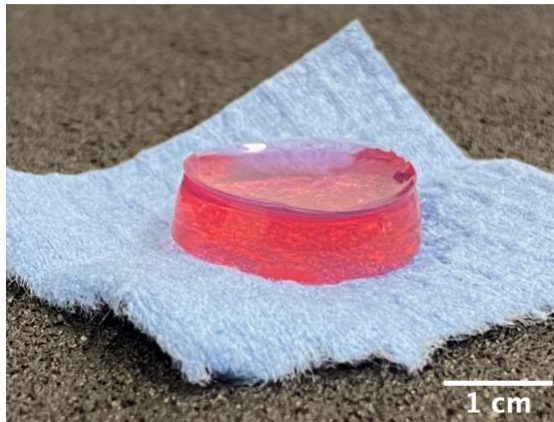
Figure 27: A crosslinked cylindrical polymer specimen resting on a piece of paper towel after being subjected to cell culture conditions for 12 days.

To further understand the system, it was important to identify which polymers were leaving the specimens at different stages of the degradation process. The matrix phase consists of 20 wt.% sucrose, 5 wt.% gelatin, and 2 wt.% alginate that is crosslinked with 0.1 M CaCl$_2$. Since the alginate is crosslinked, it was hypothesized that gelatin and sucrose were the main components leaving the matrix. Figure 28 displays the results for percent mass degradation vs. time for the matrix phase combination without sucrose.
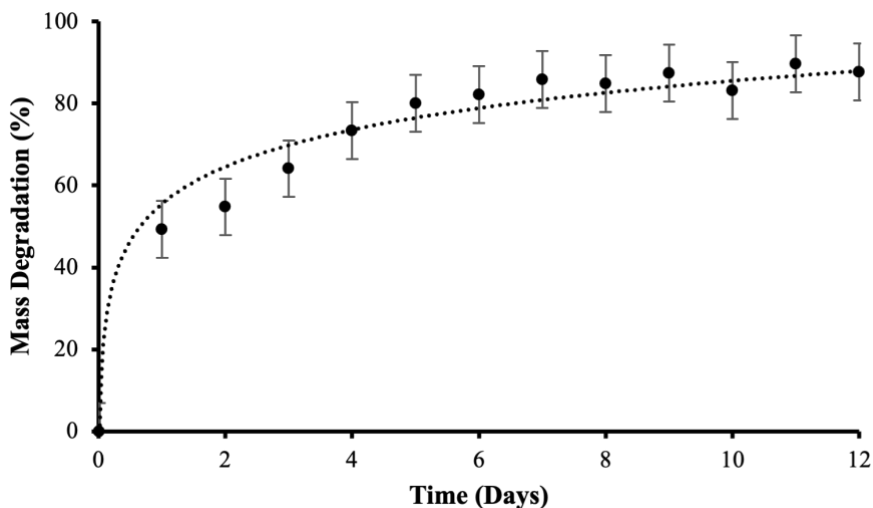
Figure 28: Percent mass degradation versus time in days for the matrix phase combination of 5 wt.% gelatin, 2 wt.% alginate crosslinked with 0.1 M CaCl$_2$. Experiments were run in triplicate to validate results, N=3.
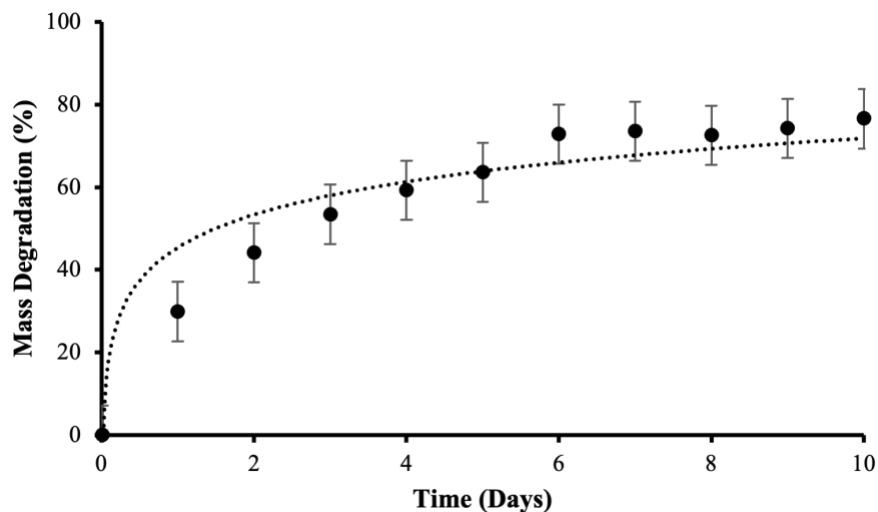
There is an initial mass loss of 30% after just 1 day of incubation which continues to increase until day 5-6 where it begins to plateau around 70% mass loss. The experiment performed without sucrose resulted in the same overall trend, but 20% lower. The difference of 20% between both experiments is undoubtedly due to the addition of 20 wt.% sucrose to the matrix phase. Since sucrose is very soluble, the majority of the sucrose is dissolved out of the specimen by the first day and very little, if any, remains in the specimen for the rest of the experiment. However, even in the sample without sucrose, there was still a 30 wt.% mass loss observed.

The next compound of interest for mass loss was gelatin. Gelatin is required for proper formation of the hydrogel matrix. Therefore, I had to determine a different method of analyzing the mass loss of gelatin within the system. If gelatin was leaving the specimens, it would be present in the media. Each day, the media in each well was removed and replaced with fresh media. Knowing that gelatin gels when cooled, I began collecting the

60

media surrounding the specimens each day and placed them at 4 °C. For the first three days, the media completely solidified indicating large amounts of gelatin were leaving the specimens and entering the media. The media removed on days 4-5 began to act more like a liquid with dispersed chunks of solidified gelatin, and by day 6 the media taken off did not contain any gelatin (as indicated by similar viscosity and appearance to fresh culture media).

These findings correlate with the mass loss trends observed in Figure 26 and Figure 28. Thus, the initial mass loss on day one is likely due to the 20 wt.% sucrose and a large amount of the gelatin present in the sample, whereas days 2-5 are due to the further mass loss of gelatin throughout the sample which tapers off around day 6. The mass loss from day 6 and onward reaches a plateau and remains very consistent suggesting that the crosslinked alginate structure is well maintained.

4.2.3 Compression Testing

The matrix phase of 5 wt.% gelatin and 2 wt.% alginate crosslinked using 0.1 M $CaCl_2$ was tested under compression until its breaking point. Figure 29 displays the stress-strain curve for one of these samples.

Figure 29: Stress vs. strain curve for a cylindrical specimen composed of 5 wt.% gelatin and 2 wt.% alginate crosslinked using 0.1 M CaCl$_2$.

These experiments indicated a peak stress before failure of around 900 kPa before the sample fractured, which is incredibly high. When handling the samples, they were comparable to polydimethylsiloxane (PDMS). Considering these polymers will be used for soft tissue applications including cell culture, a material of this durability would not be suitable. However, addition of sucrose to the matrix phase had a large impact on the mechanical properties. Figure 30 displays the stress-strain curve and sample fracture for a matrix phase composed of 20 wt.% sucrose, 5 wt.% gelatin and 2 wt.% alginate crosslinked using 0.1 M CaCl$_2$.
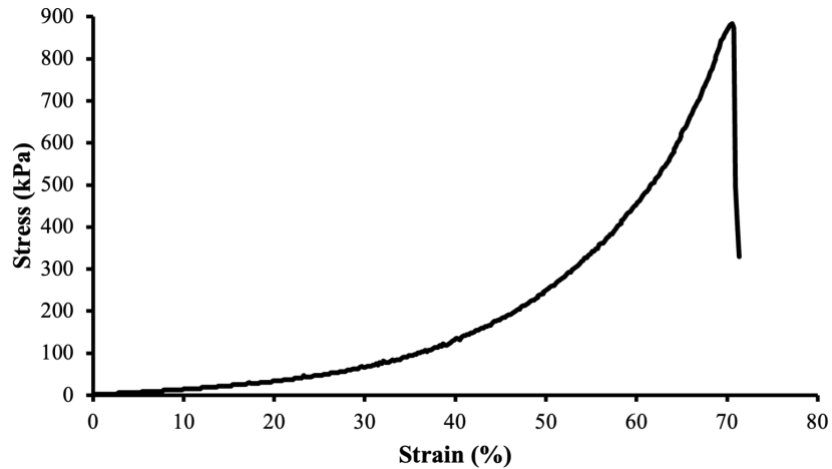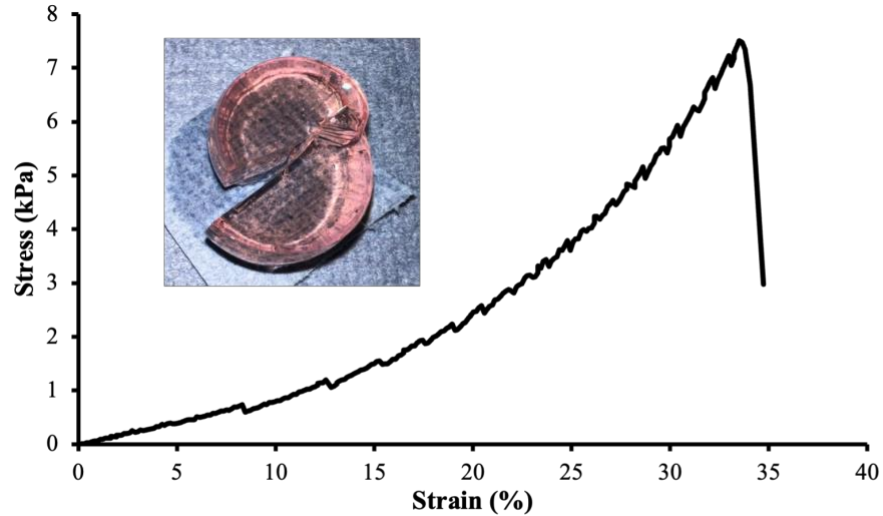
Figure 30: The average stress vs. strain curve for a cylindrical specimen composed of 20 wt.% Sucrose, 5 wt.% gelatin, and 2 wt.% alginate crosslinked using 0.1 M CaCl$_2$. The type of sample fracture is also shown in the graph. Experiments were run in triplicate to validate results, N=3.

The peak stress recorded before failure for these samples was around 8 kPa which is considerably lower than the 900 kPa observed for the samples without sucrose. Addition of sucrose to the matrix phase decreased the total stress by almost 100-fold. It is possible that the sucrose increased the porosity of the material and as porosity of a hydrogel increases, the compressive load of that material should decrease (Hwang, et al., 2010). The compressive modulus was measured between 0-10% to account for the magnitude of strain cells exert on their surroundings. The compressive modulus between 1-10% strain is 8 kPa calculated using Eq. 2 which is the slope of the stress-strain curve between 1-10% strain.

$$\textbf{\textit{Compressive modulus}} = \frac{\Delta \textbf{\textit{Stress}}}{\Delta \textbf{\textit{Strain}}} \qquad \text{Eq. 2}$$

For reference, the compressive modulus of brain tissue ranges from 0.1-10 kPa (Singh & Chanda, 2021). The compressive modulus of the matrix phase is within range for soft tissue brain matter and therefore would be a suitable application for tissue models regarding

studies of the brain. It is also important to note that the modulus of this material can be altered by changing the crosslinker concentration.

4.2.4 Cell Viability

Cell viability assays were run in triplicate and analyzed at 24 and 48 hours of culturing LUHMES embryoid bodies evenly distributed throughout a cylindrical crosslinked matrix phase specimen of 5 mm in height and 22.8 mm in diameter. LUHMES cells seeded directly onto tissue culture plastic was used as the control for this experiment to compare the cell viability between both data sets.
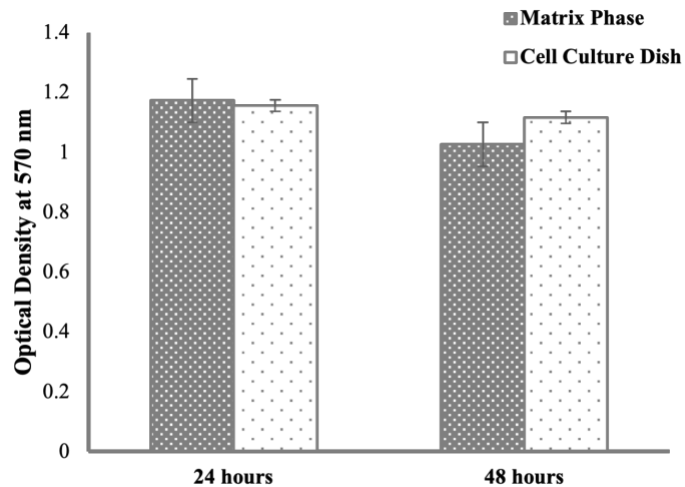
Figure 31: MTT assay results at 24 and 48 hours of culturing LUHMES embryoid bodies evenly distributed throughout a cylindrical crosslinked matrix phase specimen of 5 mm in height and 22.8 mm in diameter and directly on tissue culture plastic. The shaded bars indicate optical density of formazan solution taken from samples suspended within the matrix phase whereas the white bars indicate the control of LUHMES cells grown on tissue culture plastic. Statistical analysis of the resulting data confirmed no statistical significance between data sets. N=3 for both 24 and 48 hour experiments.

The MTT assay results displayed in Figure 31 confirm the finalized matrix phase supports growth of LUHMES cells without any acute cytotoxicity. Additionally, a one way ANOVA test confirmed no statistical significance between data sets. The optical density

64

after 24 hours of culturing for LUHMES cells grown in the matrix phase and on tissue culture plastic were 1.17 and 1.16, respectively. Additionally, at 48 hours of culturing, the optical density values were 1.02 and 1.12, respectively. These results suggest that the matrix used in this study may be suitable for neural tissue engineering.

4.3 Chapter Summary

The rheology, mechanical properties, mass loss characteristics and cell viability of the matrix phase were analyzed. Rheology experiments determined the impact of temperature variations on viscosity, storage modulus, and loss modulus of the ink and matrix phase. Gelation and melting temperatures of the matrix were determined by analyzing the rheology data. Additionally, viscosity values of the ATPS provided information about the shape fidelity and print stability of a printed structure. Although the ATPS formulation for this project was suitable for printing hollow microchannels inside a hydrogel matrix, there were some aspects of the system that could be improved upon. As described in section 4.2.1, the viscosity of the ink phase was considerably lower than the viscosity of the matrix phase. Although this ATPS combination was capable of forming channels, increasing the viscosity of the ink phase would greatly increase fidelity and print stability of the resulting channels. Additionally, a higher viscosity ink could be printed at faster translation speeds while maintaining uniformity, reducing overall printing times, thus potentially mitigating premature gelling of the matrix phase.

The matrix phase was analyzed for its mechanical properties and mass loss characteristics. Through a series of compression tests, the average compressive elastic modulus of the material was found to be 8 kPa, confirming the suitability for modelling soft tissues. Additionally, mass loss data provided insight on how the material will hold up

in cell culture conditions. The initial loss of sucrose likely increases the overall porosity of the material, potentially allowing for greater access to nutrients to cells and easier removal of waste products. The loss of gelatin, however, it less desirable. Gelatin is used as a tool for solidifying the matrix phase after printing. Once crosslinked, alginate is responsible for maintaining the shape of the matrix phase and degradation of gelatin does not impact the overall structure. However, the steep degradation of gelatin in the first 3-5 days could pose a problem for cell attachment. One way to combat this issue would be to introduce a gelatin crosslinker, such as genipin, to decrease the degradation of gelatin.

Cell viability was analyzed through an MTT assay of LUHMES embryoid bodies cultured in the matrix phase and on tissue culture plastic. The results of the MTT assay confirmed the matrix phase supported growth of LUHMES cells without any acute cytotoxicity. Overall, experiments outlined in this section confirm the applicability for RL3DP of soft tissue models. More specifically, this combination is suitable for soft tissue applications such as blood brain barrier research, gastrointestinal, vasculature, lung, kidney, and many other types of soft tissues, which rely on a soft matrix and the presence of vasculature-like structures.

Chapter 5:   Future Directions, Model Applications, and Concluding Remarks

5.1   Future Directions

5.1.1   Complex Channel Design

This project focuses on developing and analyzing an ink and matrix phase capable of printing straight line channels. However, one could argue that hollow straight channels inside a hydrogel could be achieved by casting and crosslinking the matrix phase around a pin. This is true, however, models created using this technique are limited to a uniform diameter straight line channel geometry. The benefits of creating a model using RL3DP include precise control of channel diameter, ability to vary channel diameters over a single print, and more complex designs creating an interconnected network of channels. These advantages would create models that better represent the true vasculature observed *in vivo*. Preliminary testing of printing complex channel designs identified dragging of previously printed channels through the matrix phase when trying to print a more complex branching network. Potential solutions to resolve this issue could include increasing the viscosity of the matrix phase to reduce dragging, decreasing printing speed, or altering the temperature of system during printing.

5.1.2   Incorporation of Cells into Tissue Model

Cell viability assays indicated no acute cytotoxicity of the matrix phase. Future directions might include more extensive cell culture characterization potentially using primary cells. Future work regarding incorporation of cells into the model would include di- and tri-culture experiments. Seeding the matrix phase and the channel with different cell types would allow cells to exist in direct contact along the entire length of the channel.

For potential BBB modelling, the matrix phase could be seeded with CNS cells (astrocytes, pericytes, and neuronal precursor cells) and the channel could be seeded with brain microvascular endothelial cells. Continuous flow of media through the channel and the direct cell-cell contact between the endothelium and CNS cells would hold potential to better represent the native BBB. Additionally, the printed channel could be coated with ECM proteins to increase attachment and barrier function of the endothelial cells.

5.1.3   Scaling up the RL3DP Process

The Thorlabs motors used to build the RL3DP setup have a maximum range of 25 mm. Therefore, the length of printed channels was limited by this constraint. Future applications of RL3DP for soft tissue modelling should consider scaling up the RL3DP setup to allow for creation of longer channels as well as more complex 3D designs. The current design of the printing chamber is suitable for analyzing straight-line channels. However, design of the printing chamber can easily be altered to accommodate larger print designs. Additionally, this project only analyzed channels printed along the same plane. There were no vertical heigh difference along the length of the channel. Scaling up of the RL3DP setup would provide users with the possibility of creating larger more complex designs.

5.2   Model Applications

As briefly discussed in the introductory chapter, RL3DP of soft tissue models can be utilized over a wide range of applications. The platform provides a means of producing customized models to suit different applications. The significance of this research is mainly focused on pharmacokinetic drug research for therapeutic treatment of diseases. Pharmacokinetics is the study of the journey a pharmaceutical drug takes throughout the body. It consists of monitoring drug levels within specific organs to ensure the drug is being

absorbed and behaving properly, as well as to study the release rate of certain drugs to ensure therapeutic effectiveness and minimize risk of toxicity (Riviere, 2011). However, creating accurate *in vitro* models that possess specific disease characteristics could allow for faster throughput testing of potential drug candidates for treatment of said diseases. Pharmacokinetics is particularly useful for the study of drugs able to penetrate through the BBB and into the CNS (McGregor, Doolittle, Youngers, Bell, & Neuwelt, 2019). The endothelial barrier integrity can be evaluated through permeability assays utilizing fluorescently labeled fluids such as Lucifer Yellow (LY), Quercetin, and fluorescently labeled dextrans of different molecular weights (Grifno, et al., 2019) (Brown, et al., 2019). However, this is not the only applicable area of research. This versatile modelling technique could be applied to numerous areas of research such as cardiovascular disease, analysis of cancer development and metastasis, and even pulmonary research. The degree of crosslinking can be altered to produce a matrix phase of various stiffness values, producing a broader range of applications.

5.3 Concluding Remarks

In this thesis, a novel modelling technique utilizing an ATPS ink and matrix phase printed using a RL3DP was developed for soft tissue scaffolding. The ink and matrix phase combination developed in this thesis project is capable of producing microchannels ranging from 100-1500 μm in diameter inside a crosslinked biocompatible hydrogel. Density, phase separation, and interfacial tension fluid characteristics were fine-tuned to develop a system capable of creating neutrally buoyant and uniform channels which maintain shape after gelation and crosslinking of the matrix phase. Mass loss and compression testing experiments of the matrix phase produced promising results for soft tissue engineering

applications. Mass loss likely increases the porosity of the hydrogel, allowing for better access of nutrients and removal of waste products. Additionally, degradation of the matrix phase while still maintaining shape allows more space for the cells to grow and proliferate into the matrix phase. Although the matrix loses a substantial amount of mass, it maintains the same cylindrical shape and durability over the degradation period. The majority of the degradation is due to the presence of sucrose in the matrix phase, which increases the overall degradation percentage by 20%. The rest of the degradation is originating from the gelatin present in the sample. To reduce overall mass degradation, crosslinking of gelatin using genipin could be employed. Compression testing experiments of the matrix phase yielded an elastic modulus of 8 kPa, confirming its applicability in soft tissue engineering applications. For potential applications outside of soft tissue, the degree of crosslinking can be altered to create a matrix phase with higher modulus values. Lastly, cell viability assays confirmed no acute toxicity of the matrix phase to cells. Overall, this thesis outlines the key concepts and experiments performed to develop an ATPS ink and matrix phase capable of employing RL3DP techniques for viable tissue models.

Works Cited

Abbott, J. N. (2013). Blood–brain barrier structure and function and the challenges for CNS drug delivery. *Journal of Inherited Metabolic Disease*, 437-449.

Agarwal, R., Ko, K. R., Gratzer, P. F., & Frampton, J. P. (2017, May 15). Biopatterning of Keratinocytes in Aqueous Two-Phase Systems as a Potential Tool for Skin Tissue Engineering. *MRS Advances, 2*, 2443-2449.

Albertsson, P.-Å. (1995). *Aqueous Biphastic Systems. Properties and Applications in Bioseparation.* Berlin: Springer.

Antonov, Y. A., Puyvelde, P. V., & Moldenaers, P. (2004, December 17). Interfacial tension of aqueous biopolymer mixtures close to the critical point. *Journal of Biological Macromolecules*(34), 29-35.

Asenjo, J. A., & Andrews, B. A. (2011, December 9). Aqueous two-phase systems for protein separation: a perspective. *Journal of Chromotography A, 1218*(49), 8826-8835.

Becker, M., Gurian, M., Schot, M., & Jeroen, L. (2022, December 30). Aqueous Two-Phase Enabled Low Viscosity 3D (LoV3D) Bioprinting ofLiving Matter. *Advanced Science*(2204609).

Bello, A. B., Kim, D., Kim, D., Park, H., & Lee, S.-H. (2020). Engineering and Functionalization of Gelatin Biomaterials: From Cell Culture to Medical Applications. *Tissue Engineering & Regenerative Medicine International Society*, 164 - 180.

Bishop, E. S., Mostafa, S., Pakvasa, M., Luu, H. H., Lee, M. J., Wolf, J. M., . . . Reid, R. R. (2017, November 22). 3-D bioprinting technologies in tissue engineering and regenerative medicine: Current and future trends. *Genes & Diseases, 9*(6), 185-195.

Brown, J. A., Pensabene, V., Markov, D. A., Allwardt, V., Neely, D., Shi, M., . . . Bowman.
(2015). Recreating blood-brain barrier physiology and structure on chip: A novel
neurovascular microfluidic bioreactor. *Biomicrofluidics*, 1-16.

Brown, T. D., Nowak, M., Bayles, A. V., Prabhakapandian, B., Karande, P., Lahann, J., . .
. Miitragotri, S. (2019). A microfluidic model of human brain (µHuB) for
assessment of blood brain barrier. *Bioengineering & Translational Medicine*.

Cardiovasculature disease. (2023). Retrieved from World Health Organization:
https://www.who.int/health-topics/cardiovascular-diseases#tab=tab_1

Chan, L., Jin, Y., & Heng, P. (2002, August). Cross-linking mechanisms of calcium and
zinc in production of alginate microspheres. *International Journal of
Pharmaceutics, 242*(1-2), 255-258.

Chao, Y., & Shum, H. C. (2020). Emerging aqueous two-phase systems: From
fundamentals of interfaces to biomedical applications. *Royal Society of Chemistry*,
114 - 142.

Cucullo, L., Hossain, M., Puvenna, V., Marchi, N., & Janigro, D. (2011). The role of shear
stress in Blood-Brain Barrier endothelial physiology. *BMC Neuroscience*, 1471 -
2202.

Cumings, J., Lee, G., Ritter, A., Sabbagh, M., & Zhong, K. (2020). Alzheimer's disease
drug development pipeline: 2020. *Translational Research & Clinical Inventions*.

Dillekas, H., Rogers, M. S., & Straume, O. (2019, July 25). Are 90% of deaths from cancer
caused by metastases? *Cancer Medicine, 8*, 5574-5576.

Djagny, K. B., Wang, Z., & Xu, S. (2001). Gelatin: A Valuable Protein for Food
andPharmaceutical Industries: Review. *Critical Reviews in Food Science and
Nutrition, 41*(6), 481 - 492.

Duconseille, A., Wein, F., Audonnet, F., Traore, A., Refregiers, M., Astruc, T., & Santé - Lhoutellier, V. (2017, December 6). The effect of origin of the gelatin and ageing on the secondary structure and water dissolution. *Food Hydrocolloids, 66*, 378 - 388.

Duval, K., Grover, H., Han, L.-H., Mou, Y., Pegoraro, A. F., Fredberg, J., & Chen, Z. (2017). Modeling Physiological Events in 2D vs. 3D Cell Culture. *Review: Physiology*, 266 - 277.

Edwards, T. G., & Bloom, D. C. (2019, March). Lund Human Mesencephalic (LUHMES) Neuronal Cell Line Supports Herpes Simplex Virus 1 Latency In Vitro. *Journal of Virology, 93*(6), 10-18.

Faber, T. (2022, August 8). *Britannica.* Retrieved from Fluid mechanics: https://www.britannica.com/science/fluid-mechanics

Field, R. D., Jakus, M. A., Chen, X., Human, K., Zhao, X., Chitnis, P. V., & Sia, S. K. (2022, March 01). Ultrasound-Responsive Aqueous Two-Phase Microcapsules for On-Demand Drug Release. *Angwandte, 134*(20).

Frerix, A., Müller, M., Kula, M.-R., & Hubbuch, J. (2010, December 23). Scalable recovery of plasmid DNA based on aqueous two-phase separation. *Biotechnology and Applied Biochemistry, 42*(1), 57-66.

Gaugler, J., James, B., Johnson, T., Reimer, J., Solis, M., & Weuve, J. (2022). *Alzheimer's Diseases Facts and Figures.* Chicago: Alzheimers Association.

Grifno, G. N., Farrell, A. M., Linville, R. M., Arevalo, D., Kim, J. H., Gu, L., & Searson, P. C. (2019). Tissue-engineered blood-brain barrier models via directed differentiation of human induced pluripotent stem cells. *Scientific Reports, 9*.

Gungon-Ozkerim, S., Inci, I., Zhang, Y. S., Khademhosseini, A., & Dokmeci, M. R. (2018, January 12). Bioinks for 3D bioprinting: an overview. *Royal Society of Chemistry, 6*(5), 915-946.

Hajash, K., Sparrman, B., Guberan, C., Laucks, J., & Tibbits, S. (2017). Large - Scale Rapid Liquid Printing. *3D Printing and Additive Manufacturing, 4*, 123-131.

He, Y., Yao, Y., Tsirka, S. E., & Cao, Y. (2014). Cell - Culture Models of the Blood - Brain Barrier . *Stroke*, 2514 - 2526.

Helmiyati, & Aprilliza, M. (2017). Characterization and properties of sodium alginate from brown algae used as an ecofriendly superabsorbent. *Materials Science and Engineering. 188.* IPO Publishing.

Hossain, A., Munir, S., & Pop, I. (2001). Natural convection flow of a viscous fluid with viscosity inversely proportional to linear function of temperature from a vertical wavy cone. *International Journal of Thermal Sciences*, 366 - 371.

Hwang, C. M., Sant, S., Masaeli, M., Kachouie, N. N., Zamanian, B., Lee, S.-h., & Khademhosseini, A. (2010, Spetember 8). Fabrication of three-dimensional porous cell-laden hydrogel for tissue engineering. *International Society for Biofabrication, 2.*

Iffah, Z., Arshad, M., & Amid, A. (2018). Procedure to Develop Binodal Curve and Phase Diagram for Aqueous Two-Phase System. In A. Amid, S. Sulaiman, D. N. Jimat, N. Fadillah, & M. Azmin, *Multifacteted Protocol in Biotechnology.* Singapore, Asia: Springer.

Iqbal, M., Tao, Y., Xie, S., Zhu, Y., Chen, D., Wang, X., . . . Yuan, Z. (2016, October 28). Aqueous two-phase system (ATPS): an overview and advances in its applications. *Biological Procedures Online, 18*(18).

Jaber, N. (2022, May 27). *Cancer in Lymph Nodes May Help Tumors Spread by Enlisting Immune Cells*. Retrieved from National Cancer Institute: https://www.cancer.gov/news-events/cancer-currents-blog/2022/cancer-lymph-nodes-metastasis

Kaisar, M. A., Sajja, R. K., Prasad, S., Abhyankar, V. V., Liles, T., & Cucullo, L. (2016). New experimental models of the blood - brain barrier for CNS drug discovery. *Expert Opinion on Drug Discovery*, 89 - 103.

Ko, H., Ratri, M. C., Kim, K., Jung, Y., Tae, G., & Shin, K. (2020). Formulation of Sugar/Hydrogel Inks for Rapid Thermal Response 4D Architectures with Sugar-derived Macropores. *Scientific Reports*.

Lazzari, S., Maggioni, G. M., soos, M., Wu, H., & Morbidelli, M. (2013, October 16). Shear-stability and gelation of inverse latexes. *The Royal Society of Chemistry 2013, 9*, 10866 - 10876.

Legna, R. E. (1988). The Sigma-Aldrich library of chemical safety data. (R. E. Legna, Ed.) Milwaukee, Wisconsin, USA.

Limbu, Y. R., Grung, G., Handari, R., & Regmi, S. R. (2006). Assessment of carotid artery dimensions by ultrasound in non-smoker healthy adults of both sexes. *National Library of Medicine*.

Logan, S., Arzua, T., Canfield, S. G., Seminary, E. R., Sison, S. L., Edbert, A. D., & Bai, X. (2019). Studying Human Neurological Disorders Using Induced Pluripotent Stem Cells: From 2D Monolayer to 3D Organoid and Blood Brain Barrier Models. *Comprehensive Physiology*, 565-611.

Matsa, E., Burridge, P. W., & Wu, J. C. (2014, June 4). Human Stem Cells for Modeling Heart Disease and for Drug Discovery. *Science Translational Medicine, 6*(239).

McGregor, J. M., Doolittle, N. D., Youngers, E., Bell, S. D., & Neuwelt, E. A. (2019). Pharmacokinetics of Drug Delivery Past the Blood - Brain Barrier. In *Nervous System Drug Delivery* (pp. 57 - 72). Academic Press.

Menefee, W., Jenks, J., Mazzasette, C., & Nguyen, K. L. (2021). Structure and Function of Blood Vessels. *LibreTexts Medicine*.

Metastatic Cancer: When Cancer Spreads . (2020, November 10). Retrieved from National Cancer Institute: https://www.cancer.gov/types/metastatic-cancer

Monson, K. L., Goldsmith, W., Barbaro, N. M., & Manley, G. T. (2005). Significance of source and size in the mechanical response od human cerebral blood vessels. *Journal of Biomechanics, 38*, 737-744.

Negheih, S., & Chen, X. (2021, February 10). Printability: A key issue in extrusion-based bioprinting. *Journal of Pharmaceutical Analysis, 11*(5), 564-579.

Nelson, A. R., Sweeney, M. D., Sagare, A. P., & Zlohovic, B. V. (2015). Neurovascular dysfunction and neurodegeneration in dementia and Alzheimer's disease. *BBA Molecular Basis of Disease*, 1 - 15.

Osorio, F. A., Bilbao, E., Bustos, R., & Alvarez, F. (2007, November 20). Effects of Concentration, Bloom Degree, and pH on Gelatin Melting and Gelling Temperatures Using Small Amplitude Oscillatory Rheology. *International Journal of Food Properties, 10*, 841-851.

Palmiotti, C. A., Prasad, S., Naik, P., Abul, K. M., Sajja, R. K., Achyuta, A. H., & Cucullo, L. (2014). In Vitro Cerebrovascular Modeling in the 21st Century: Current and Prospective Technologies. *Springer Science*, 3229 - 3250.

Pardridge, W. M. (2012). Drug Transport across the blood - brain barrier . *Journal of Cerebral Blood Flow and Metabolism*, 1959 - 1972.

Park, T. -E., Mustafaoglu, N., Herland, A., Hasselkus, R., Mannix, R., FitzGerald, E. A., . . . Goumnerova, L. C. (2019). Hypoxia-enhanced Blood-Brain Barrier Chip recapitulates human barrier function and shuttling of drugs and antibodies. *Nature Communications*, 1 - 12.

Parker, K. K., & Ingber, D. E. (2007, June 22). Extracellular matrix, mechanotransduction and structural hierarchies in heart tissue engineering. *Philosophical Translations of the Royal Socirty B: Biological Sciences, 362*(1484), 1267-1279.

Peacock, C. J., Lamont, C., Sheen, D. A., Shen, V. K., Kreplak, L., & Frampton, J. P. (2021). Predicting the Mixing Behavior of Aqueous Solutions using a Machine Learning Framework. *Applied Materials & Interfaces, 13*(9), 11449-11460.

Riviere, J. E. (2011). *Comparitive Pharmacokinetics: Principles, techniques & applications.* Iowa: Blackwell's Publishing.

Santaguida, S., Janigro, D., Hossain, M., Oby, E., Rapp, E., & Cucullo, L. (2006). Side by side comparison between dynamic versus static models of blood–brain barrier in vitro: A permeability study. *Brain Research*, 1 - 13.

Serlin, Y., Shelef, I., Knyazer, B., & Friedman, A. (2015). Anatomy and physiology of the blood–brain barrier. *Seminars in Cell & Developmental Biology*, 1-5.

Shao, X., Gao, D., Chen, Y., Jin, F., Hu, G., Jiang, Y., & Liu, H. (2016). Development of a blood-brain barrier model in a membrane-based microchip for characterization of drug permeability and cytotoxicity for drug screening. *Analytica Chimica Acta, 934*, 186 - 193.

Singh, G., & Chanda, A. (2021, October 19). Mechanical properties of whole - body soft human tissue: a review. *Biomedical Materials, 16*.

Sivandzade, F., & Cucullo, L. (2018). In-vitro blood–brain barrier modeling: A review of modern and fast-advancing technologies. *Journal of Cerebral Blood Flow & Metabolism*, 1-15.

Sreekumar, K., & Baby, B. (2020). Alginic Acid: a Potential Biopolymer from Brown Algae. *Materials International*, 433 - 438.

van der Graaf, S., Schroën, C., van der Sman, R., & Boom, R. (2004, June 1). Influence of dynamic interfacial tension on droplet formation during membrane emulsification. *Journal of Colloid and Interface Science, 277*, 456 - 463.

Wood, L. (2021, April 12). *Research and Markets: The Worlds Largest Market Research Store*. Retrieved from Intrado Globe News wire: https://www.globenewswire.com/en/news-release/2021/04/12/2207999/28124/en/Global-Rapid-Liquid-Printing-Market-2021-to-2026-by-Offering-Application-Industry-and-Geography.html

Zang, X.-m., Yin, M., & Zhang, M.-h. (2014). Cell-based assays for Parkinson's disease using differentiated human LUHMES cells. *Nature*(35), 945-956.

Zhang, X., Zong, W., Bi, H., Zhao, K., Fuhs, T., Hu, Y., . . . Han, X. (2018, February 16). Hierarchical drug release of pH-sensitive liposomes encapsulating aqueous two phase system. *European Journal of Pharmaceutics and Biopharmaceutics, 127*, 177-182.
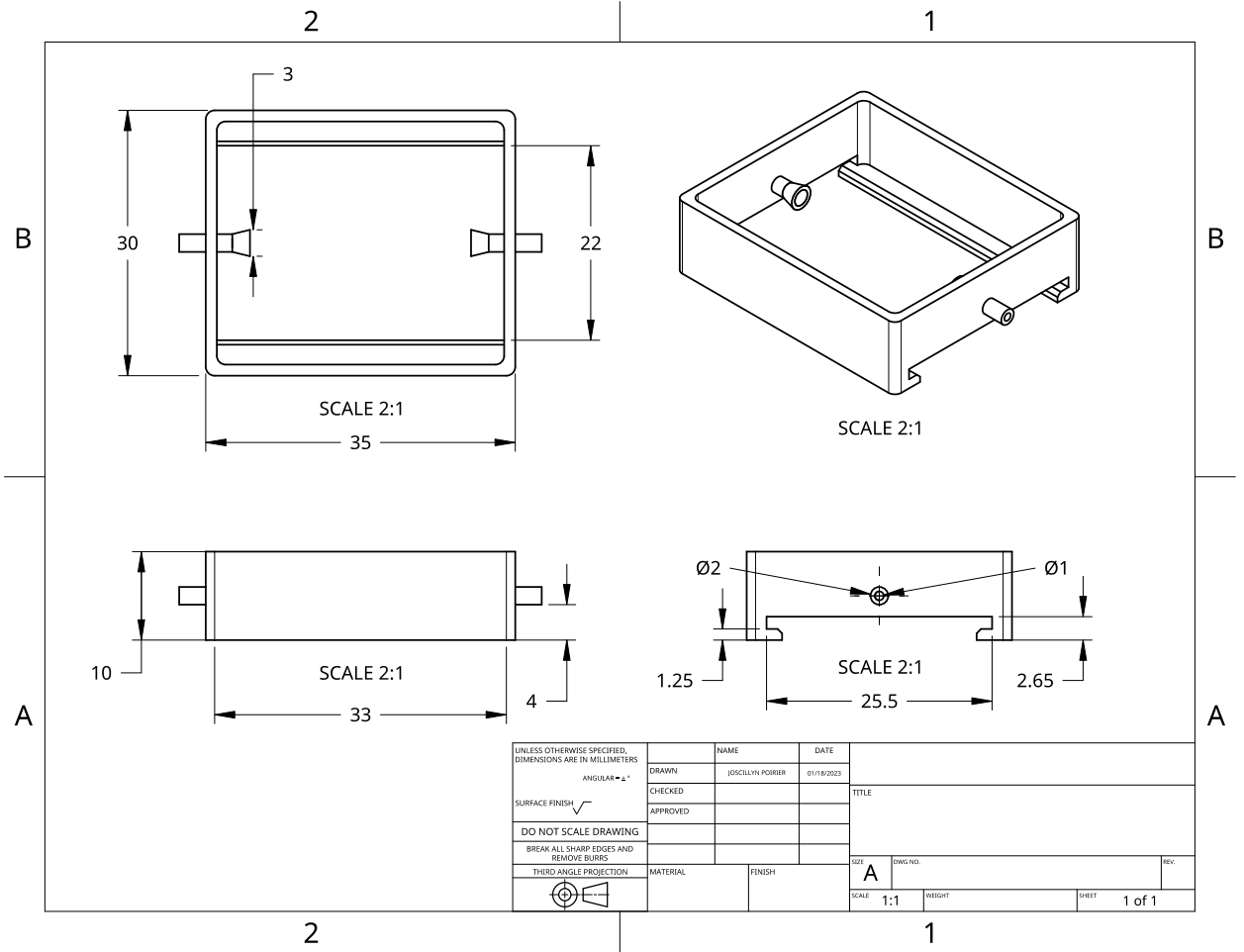
Appendix A: Supplementary Figures

Figure A1: Engineering drawing of the printing chamber showing the dimensions and size of the final design.

Appendix B: Supplementary Tables

Table B1: Print settings used for the ChiTuBox slicing software.

Setting	Input	Setting	Input
Layer Height	0.05 mm	Bottom Lift Distance	5 mm
Bottom Layer Count	2	Lifting Distance	5 mm
Exposure Time	3 seconds	Bottom Lift Speed	60 mm/min
Light – off Delay	0 seconds	Lifting Speed	80 mm/min
Resin Density	1.1 g/ml	Retract Speed:	210 mm/min

Table B2: Overview of process performed to finalize ink and matrix phase compositions.

#	Polymer (wt.%)					Outcomes/Issues Encountered	Next Modification
	Gel.	Alg.	PEG	PEO	Suc.		
1	10	2	17.5	0.1	-	• Interfacial tension too high, channel breakup. • Density imbalance, ink would rise.	• Increased conc. of PEO to see impact.
2	10	2	17.5	1	-	• Channel breakup. • Density imbalance. • High PEO conc. produced a viscous, stringy ink phase. The ink dragged through the matrix phase, not good for complex prints.	• Halved conc. of PEO to 0.5wt.%.
3	10	2	17.5	0.5	-	• Channel breakup. • Density imbalance. • Ink phase still too viscus and stringy.	• Lowered conc. of PEO back to 0.1wt.%. • Lowered PEG concentration to combat interfacial tension.
4	10	2	10	0.1	-	• Interfacial tension lowered, but still causing breakup. • Density imbalance.	• Based on binodal, conc. of gelatin was halved to 5wt.% and conc. Of PEG was decreased to 2.5wt.%.
5	5	2	2.5	0.1	-	• Interfacial tension very small, formed properly with no channel breakup. • Density imbalance.	• Temp. vs. density vs. conc. experiments for PEG, PEO, Alg. Gel. (Figure 10). • Too many factors involved to efficiently optimize polymer conc. • When polymer conc. was altered, re-optimization of system was required. • Sucrose introduced to eliminate density constraint.
6	5	2	2.5	0.1	10 20 30	• Same conc. of sucrose in ink and matrix phase still had density imbalance. • Tested different sucrose conc. for Ink/Matrix (ex. 10/20, 10/30, 20/10, 20/30, 30/10, **30/20**).	• Determined that 20wt% sucrose in matrix and 30wt.% sucrose in ink phase equilibrized density. • No sinking or floating, remained neutrally buoyant and uniform.

Appendix C: Copyright Information

About this article

Cite this article

Park, TE., Mustafaoglu, N., Herland, A. *et al.* Hypoxia-enhanced Blood-Brain Barrier Chip recapitulates human barrier function and shuttling of drugs and antibodies. *Nat Commun* **10**, 2621 (2019). https://doi.org/10.1038/s41467-019-10588-0

Check for updates

http://creativecommons.org/licenses/by/4.0/

See next page

82

MARY ANN LIEBERT, INC. LICENSE
TERMS AND CONDITIONS

Feb 17, 2023

This Agreement between Dalhousie University -- Joscillyn Poirier ("You") and Mary Ann
Liebert, Inc. ("Mary Ann Liebert, Inc.") consists of your license details and the terms and
conditions provided by Mary Ann Liebert, Inc. and Copyright Clearance Center.

License Number	5491401409444
License date	Feb 17, 2023
Licensed Content Publisher	Mary Ann Liebert, Inc.
Licensed Content Publication	3D Printing and Additive Manufacturing
Licensed Content Title	Large-Scale Rapid Liquid Printing
Licensed Content Author	Kathleen Hajash, Bjorn Sparrman, Christophe Guberan, et al
Licensed Content Date	Sep 1, 2017
Licensed Content Volume	4
Licensed Content Issue	3
Type of Use	Dissertation/Thesis
Requestor type	author of the original work

Format	print and electronic
Portion	figures/tables
Number of figures/tables	1
Distribution quantity	5
Title	Rapid Liquid 3D – Printing of Microchannels using Aqueous Two – Phase Systems for Tissue Modelling Applications
Institution name	Dalhousie University
Expected presentation date	Mar 2023
Portions	Figure 2 A and B on page 125
Requestor Location	Dalhousie University 5651 Ogilvie Street, suite 915 Halifax, NS B3H 1B9 Canada Attn: Dalhousie University
Total	0.00 CAD

Terms and Conditions

Mary Ann Liebert, Inc. publishers Terms and Conditions

1. Introduction

The publisher for this copyrighted material is Mary Ann Liebert, Inc. publishers. By clicking "accept" in connection with completing this licensing transaction, you agree that the following terms and conditions apply to this transaction (along with the Billing and Payment terms and conditions established by Copyright Clearance Center, Inc. ("CCC"), at the time that you opened your Rightslink account and that are available at any time at https://myaccount.copyright.com).

2. Limited License

Publisher hereby grants to you a non-exclusive license to use this material. Licenses are for one-time use only with a maximum distribution equal to the number that you identified in the licensing process and any electronic posting is limited to the period committed to at the time of purchase.

3. Geographic Rights: Scope

Licenses may be exercised anywhere in the world.

4. Jurisdiction:

This agreement shall be governed by and construed in accordance with the laws of the state of New York, without giving effect to any principles of conflicts of law. If any provision of this agreement shall be unlawful, void, or for any reason unenforceable, then that provision shall be deemed severable from this agreement and shall not affect the validity and enforceability of any remaining provisions. This is the entire agreement between the parties relating to the subject matter herein and shall not be modified except in writing, signed by both parties.

5. Altering/Modifying Material: Not Permitted

You may not alter or modify the material in any manner without the explicit approval of the Publisher.

6. Reservation of Rights

Publisher reserves all rights not specifically granted in the combination of (i) the license details provided by you and accepted in the course of this licensing transaction, (ii) these terms and conditions and (iii) CCC's Billing and Payment terms and conditions.

7. License Contingent on Payment

While you may exercise the rights licensed immediately upon issuance of the license at the end of the licensing process for the transaction, provided that you have disclosed complete and accurate details of your proposed use, no license is finally effective unless and until full payment is received from you (either by publisher or by CCC) as provided in CCC's Billing and Payment terms and conditions. If full payment is not received on a timely basis, then any license preliminarily granted shall be deemed automatically revoked and shall be void as if never granted. Further, in the event that you breach any of these terms and conditions or any of CCC's Billing and Payment terms and conditions, the license is automatically revoked and shall be void as if never granted. Use of materials as described in a revoked license, as well as any use of the materials beyond the scope of an unrevoked license, may constitute copyright infringement and publisher reserves the right to take any and all action to protect its copyright in the materials.

8. Copyright Notice: Disclaimer

You must include the following copyright and permission notice in connection with any reproduction of the licensed material:" The publisher for this copyrighted material is Mary Ann Liebert, Inc. publishers."

9. Warranties: None

Publisher makes no representations or warranties with respect to the licensed material and adopts on its own behalf the limitations and disclaimers established by CCC on its behalf in its Billing and Payment terms and conditions for this licensing transaction.

10. Indemnity

You hereby indemnify and agree to hold harmless publisher and CCC, and their respective officers, directors, employees and agents, from and against any and all claims arising out of your use of the licensed material other than as specifically authorized pursuant to this license.

11. No Transfer of License

This license is personal to you and may not be sublicensed, assigned, or transferred by you to any other person without publisher's written permission.

12. No Amendment Except in Writing

This license may not be amended except in writing signed by both parties (or, in the case of publisher, by CCC on publisher's behalf).

13. Objection to Contrary Terms

Publisher hereby objects to any terms contained in any purchase order, acknowledgment, check endorsement or other writing prepared by you, which terms are inconsistent with these terms and conditions or CCC's Billing and Payment terms and conditions. These terms and conditions, together with CCC's Billing and Payment terms and conditions (which are incorporated herein), comprise the entire agreement between you and publisher (and CCC) concerning this licensing transaction. In the event of any conflict between your obligations established by these terms and conditions and those established by CCC's Billing and Payment terms and conditions, these terms and conditions shall control.

v1.1

Questions? customercare@copyright.com.